

1 Representing effects of aqueous phase reactions in 2 shallow cumuli in global models

Ji Nie,¹ Zhiming Kuang,^{2,3} Daniel Jacob,³ Jiahua Guo,³

3 Key points.

- 4 • A EDMF model can well reproduce the results of a LES embedded with idealized aqueous
5 reactions.
- 6 • The aqueous oxidation of SO₂ by H₂O₂ is relatively slow compared to the in-cloud residence
7 time of air parcels.
- 8 • Operator splitting between tracer transport and aqueous reactions leads to significant errors.

Corresponding author: Ji Nie, Lamont-Doherty Earth Observatory, 301E Oceanography, 61
Route 9W, Palisades, NY 10960. (jn2460@columbia.edu)

¹Lamont-Doherty Earth Observatory,

9 **Abstract.** Aqueous phase reactions are important, sometimes dominant
10 (e.g. for SO_2), pathways for the oxidation of air pollutants at the local and/or
11 global scale. In many current chemical transport models (CTMs), the trans-
12 port and aqueous reactions of chemical species are treated as split processes,
13 and the subgrid-scale heterogeneity between cloudy and environmental air
14 are not considered. Here, using Large-Eddy Simulations (LES) with ideal-
15 ized aqueous reactions mimicking the oxidation of surface-originated SO_2 by
16 H_2O_2 in shallow cumuli, we show that the eddy-diffusivity mass-flux (EDMF)
17 approach with a bulk plume can represent those processes quite well when
18 entrainment/detrainment rates and eddy diffusivity are diagnosed using a
19 conservative thermodynamic variable such as total water content. The rea-
20 son is that a typical aqueous reaction such as SO_2 aqueous oxidation is rel-
21 atively slow compared to the in-cloud residence time of air parcels in shal-
22 low cumuli. As a result, the surface-originated SO_2 is well correlated with

Columbia University, New York, New York

²Department of Earth and Planetary
Sciences, Harvard University, Cambridge,
MA, USA.

³John A. Paulson School of Engineering
and Applied Sciences, Harvard University,
Cambridge, MA, USA.

23 and behaves like conservative thermodynamic variables that also have sources
24 at the surface. Experiments with various reaction rate constants and rela-
25 tive abundances of SO_2 and H_2O_2 indicate that when the reaction timescale
26 approaches the in-cloud residence time of air parcels, the errors of the bulk
27 plume approach start to increase. Treating chemical tracer transport and aque-
28 ous reaction as split processes leads to significant errors, especially when the
29 reaction is fast compared to the in-cloud residence time. Overall, the EDMF
30 approach shows large improvement over the CTM-like treatments in match-
31 ing the LES results.

1. Introduction

32 Moist convection plays a number of roles in atmospheric chemistry including vertical
33 transport and turbulent mixing of chemical species, photochemistry (by altering the radi-
34 ation field), lightning production of NO_x , wet removal, and aqueous phase reactions. The
35 aqueous phase reactions are very important for some chemical species, a prominent exam-
36 ple being sulfur dioxide (SO_2). SO_2 has major sources from fuel combustion, ore smelting,
37 volcano eruptions, and oxidation of dimethyl sulfide (DMS) emitted by the marine bio-
38 sphere. SO_2 can be oxidized in the atmosphere, producing sulfate aerosols that affect air
39 quality, cloud nucleation, and climate [e.g. *Berg et al.*, 2011; *Ghan et al.*, 2012]. Because
40 the aqueous phase oxidation of SO_2 by H_2O_2 and O_3 is much more rapid than the gaseous
41 phase oxidation by OH , it dominates global sulfate aerosol formation (60% \sim 80%, [e.g.
42 *Barth et al.*, 2000; *Rasch et al.*, 2000; *Benkovitz et al.*, 2006; *Wang et al.*, 2011]). Thus,
43 it is important to appropriately represent this type of aqueous phase reaction in global
44 models.

45 In current chemical transport models (CTMs; and global climate models, GCMs, with
46 chemistry components), due to their coarse resolution, shallow cumuli are parameterized,
47 as are the associated aqueous phase reactions. In many CTMs [e.g. *Barth et al.*, 2000;
48 *Liu et al.*, 2005; *Jöckel et al.*, 2006; *Verma et al.*, 2007; *Wu et al.*, 2007], the transport
49 and reactions of chemical tracers are treated as split processes over a CTM time step:
50 the CTMs first use the convective mass flux to calculate the convective transport, then
51 call chemical solvers to calculate the gaseous and aqueous phase reactions. In addition,
52 the chemical solvers usually use the CTM-grid mean chemical concentrations to calculate

53 the aqueous phase reactions. The subgrid-scale heterogeneity (e.g. the difference between
54 cloudy and clear sky regions) of chemically reactive tracers and their correlations is not
55 considered. The above two simplifications are justifiable for gaseous phase reactions that
56 occur throughout a grid cell, but are less justifiable for aqueous phase reactions. Aqueous
57 phase reactions in cumuli mainly occur in cloudy updrafts, in which the concentrations
58 of chemical tracers can be quite different from the grid mean concentrations, as shown in
59 both observations [e.g. *Daum et al.*, 1984] and numerical modeling [e.g. *Kazil et al.*, 2011].
60 The cloudy updrafts also contribute to the majority of the tracer transport above the
61 subcloud layer [e.g. *Vilà-Guerau de Arellano et al.*, 2005], thereby coupling the chemical
62 transport and reactions together.

63 The objective of this study is to improve representations of aqueous phase reactions in
64 shallow cumuli in the global models, particularly to mitigate the errors due to the above
65 two simplifications. We incorporate an idealized aqueous reaction into the Large-Eddy
66 Simulations (LES) of shallow cumuli. LES has been used by many previous studies to
67 investigate the effects of convection on chemistry, e.g., the photochemical disequilibrium
68 in the dry boundary layer [*Krol et al.*, 2000], and, the transport and transformations
69 influenced by shallow cumulus [*Vilà-Guerau de Arellano et al.*, 2005; *Kim et al.*, 2012].
70 Here, the LES resolves the turbulent flow and the aqueous reaction in the shallow cumuli
71 at the cloud scale, which serves as the ground truth. The idealized chemical reaction
72 is easy to understand and can be used as a starting point for the investigation of more
73 complex chemical reactions in the future. We then assess whether a simple convective
74 parameterization (the eddy-diffusivity mass-flux approach, EDMF, with a bulk plume

75 model, simply called the EDMF model hereafter) with the aqueous reaction appropriately
76 treated can well represent both the chemical and thermodynamic aspects at the same time.

77 Most convective parameterizations are designed to represent and are validated against
78 the thermodynamic aspect of convection, such as heat and moisture, or inert chemical
79 transport. Less evaluation has been done of the chemically reactive tracers, although
80 the simulations of chemistry in global models are sensitive to the choices of convective
81 parameterizations [e.g. *Jacob et al.*, 1997; *Easter et al.*, 2004; *Lawrence and Philip*, 2005].
82 To separate out the uncertainties in representing chemistry from the uncertainties in pa-
83 rameterizing convection and clouds themselves, we diagnose the parameters of the EDMF
84 model from the LES results. The aqueous reaction is formulated within the EDMF model
85 in a way that improves upon the above two simplifications (operator splitting and ne-
86 glecting subgrid-scale heterogeneity of chemicals). We show that this representation of
87 the aqueous reaction within the EDMF model can well reproduce the LES-simulated
88 chemical aspect over a wide range of chemical regimes, thus making it an effective way to
89 represent aqueous reactions and transport in shallow cumuli. We also analyze the errors
90 of aqueous reaction in the EDMF model, which helps us understand and qualitatively
91 assess when the EDMF model is adequately accurate and when it is not.

2. Methodology and Experimental Design

2.1. the LES with Reactive Tracers

92 The shallow cumuli case is the non-precipitating oceanic trade cumulus case from the
93 undisturbed Barbados Oceanographic and Meteorological Experiment (BOMEX, *Holland*
94 *and Rasmusson* [1973]). The BOMEX shallow cumuli stayed in a steady state for 5 days
95 in the field observation without apparent complications from precipitation or large-scale

96 perturbations. It is an excellent testbed for us to focus on the chemical aspect, because
 97 the convective processes are relatively simple and well studied, . The LES is the System
 98 for Atmospheric Modeling (SAM, *Khairoutdinov and Randall* [2003]), which has been
 99 used to simulate the BOMEX case [e.g. *Siebesma et al.*, 2003; *Nie and Kuang*, 2012a]. We
 100 run SAM with a spatial resolution of 25 *m* in all directions in a domain of 6.4 *km* (*x*) \times
 101 6.4 *km* (*y*) \times 3 *km* (*z*) with doubly periodic horizontal boundary conditions, and a time
 102 step of 1 *s*. The forcing and other settings are the same as the intercomparison study of
 103 BOMEX described in *Siebesma et al.* [2003].

104 Two massless tracers, ϕ_1 and ϕ_2 with units of *ppb*, are added to the LES to mimic the
 105 aqueous oxidation of SO_2 by H_2O_2 . ϕ_1 is released from the surface with a constant flux
 106 F_{sfc,ϕ_1} . ϕ_2 , which mimics the atmospheric oxidant H_2O_2 , is relaxed to a reference profile
 107 $\phi_{2,ref}$ that is constant in height. We set the relaxation time of ϕ_2 to be 1 day based on
 108 photochemical production of H_2O_2 [*Jacob et al.*, 1990]. ϕ_1 is also relaxed to zero with
 109 a 1 day relaxation time, which may be viewed as representing gaseous phase oxidation,
 110 such as by OH [*Barth et al.*, 2000] or O_3 in sea-salt aerosols [*Alexander et al.*, 2005].
 111 The relaxation of ϕ_1 and ϕ_2 are only applied in clear sky grid cells. We limit this study
 112 to surface-originated ϕ_1 , which may be viewed as anthropogenic sources of SO_2 or other
 113 pollutants. Other possible sources, such as the oxidation of DMS, will be considered in
 114 future work.

115 ϕ_1 and ϕ_2 react in cloud droplets within cloudy grids (grid cells with cloud liquid water
 116 $q_c \geq 0.01$ *g kg*⁻¹.) The rate of the aqueous reaction can be expressed in their gaseous
 117 phase concentrations with a bulk reaction constant k :

$$118 \quad R_n = -\frac{d\phi_{1,n}}{dt} = -\frac{d\phi_{2,n}}{dt} = k\phi_{1,n}\phi_{2,n}q_{c,n}, \quad (1)$$

119 where the subscript n indicates they are for individual LES grid cells. k (with a unit
 120 of $s^{-1} \text{ ppb}^{-1}$ per $g \text{ kg}^{-1}$ of cloud liquid water, unit is omitted hereafter) is the product
 121 of the aqueous reaction rate constant in liquid water and Henry's equilibria constants
 122 (including the dissociation of SO_2 in the aqueous phase). The aqueous reaction rate
 123 constant is divided by the liquid water content, while the conversion from aqueous-phase
 124 concentrations to gas-phase concentrations are multiplied by the liquid water content.
 125 Thus, k in Eq. 1 has no dependence on $q_{c,n}$. For the aqueous oxidation of SO_2 by H_2O_2 ,
 126 k is about $1 - 2 \times 10^{-3}$ [Seinfeld and Pandis, 1998]. Its dependence on the pH value is
 127 small and neglected. As in many previous studies [e.g. Schumann, 1989; Vilà-Guerau de
 128 Arellano et al., 2005], the chemical reaction here is highly idealized. However, the minimal
 129 complexity of the chemistry allows us to better understand the influences of convection
 130 on chemistry and to improve its representation in parameterizations.

131 A control case is set up as the benchmark. The parameters F_{sfc,ϕ_1} and $\phi_{2,ref}$ de-
 132 termine the relative abundances of ϕ_1 and ϕ_2 . In the control case, we set $F_{sfc0,\phi_1} =$
 133 $0.024 \text{ ppb kg m}^{-2} \text{ s}^{-1}$ and $\phi_{2,ref0} = 0.9 \text{ ppb}$ (subscript 0 indicates the control case value),
 134 so that the concentrations of ϕ_1 and ϕ_2 are comparable in cloudy updrafts. Observations
 135 show that either SO_2 or H_2O_2 can dominate depending on the environment [Daum et
 136 al., 1984]. The control case k is set to be 10^{-3} , close to the representative value for SO_2
 137 aqueous oxidation by H_2O_2 .

138 To explore and evaluate the performance of the EDMF model in a wide range of situ-
 139 ations, two groups of experiments are carried out in addition to the control case. Cases
 140 in group 1 have the same $k = 10^{-3}$ as in the control case. However, in each case $\phi_{2,ref}$ is
 141 divided and F_{sfc,ϕ_1} is multiplied by the same factor. There are a total of 12 cases with

142 this factor varying from $\frac{1}{12}$ to 12. Experiments in this group cover SO_2 aqueous oxidation
143 in different chemical regimes, from SO_2 dominant ($\phi_{2,ref}/\phi_{2,ref0} \ll 1$) to H_2O_2 dominant
144 ($\phi_{2,ref}/\phi_{2,ref0} \gg 1$). In the second group of 12 experiments, we keep F_{sfc,ϕ_1} and $\phi_{2,ref}$ the
145 same as in the control case, but change k from 10^{-4} to 10^{-1} . Experiments in this group
146 extend our study to explore a range of aqueous phase reaction rates.

147 The initial conditions of the chemical tracers are ϕ_1 being zero and ϕ_2 being its reference
148 profile. For most of the paper, we focus on the comparison between the EDMF model
149 and the LES results in the chemical steady state to remove the dependence on the initial
150 conditions of chemical tracers. In section 3.6, we examine the first several hours after
151 initialization to examine the EDMF model's performance in chemical transient state.
152 Many LES, including SAM, can sustain a quasi-steady BOMEX convection only for several
153 hours (hours 2 – 6 after the initialization; after that the thermodynamic fields slowly drift
154 away [e.g. *Siebesma et al.*, 2003]), which is far less than the observed 5 days and too
155 short to reach a chemical steady state without appropriate initial profiles of the chemical
156 tracers. To overcome this limitation, we first run the model for two hours. We then restart
157 and run the model repeatedly from the end of hour 2 to the end of hour 6 from the same
158 restart file (saved at the end of hour 2) except with a different set of Gaussian random
159 noise applied to the temperature fields of the lowest 5 levels in each of the restarted runs.
160 The added noise has a standard deviation of 0.02K. ϕ_1 and ϕ_2 averaged over the clear
161 sky and cloudy air are calculated at each height during the last hour of a previous run.
162 Then, the clear-sky and cloudy means are assigned as the initial values of ϕ_1 and ϕ_2 in
163 the clear sky and cloudy air, respectively, of the following restarted run. We iterated this
164 procedure for more than 12 rounds (48 simulation hours) for each case, and confirmed

165 that the chemical steady state is reached. Snapshots of thermodynamic (temperature T ,
 166 total water content q_t , and others) and chemical variables (ϕ_1 , ϕ_2 , R) are saved every
 167 minute during the final run for analysis. The first 30 minutes simulation of the final run
 168 is discarded as spin-up, so that heterogeneities of ϕ_1 and ϕ_2 inside clouds and clear sky
 169 are fully developed for the analysis period.

2.2. the EDMF Model

170 The EDMF model is evaluated against the LES results. Consider the budget equation of
 171 an arbitrary tracer (ψ) horizontally averaged over the LES domain (denoted by overbar):

$$172 \quad \frac{\partial \bar{\psi}}{\partial t} = \left(\frac{\partial \bar{\psi}}{\partial t} \right)_{forcing} - \frac{1}{\rho} \frac{\partial F_\psi}{\partial z} + \bar{S}_\psi. \quad (2)$$

173 ρ is air density. The terms on the right-hand side (RHS) are the imposed large-scale forc-
 174 ing, vertical convergence of turbulent flux, and net source, respectively. For the chemical
 175 tracers, the large-scale forcing term is zero, and the source terms includes relaxation in
 176 the clear sky and the aqueous reaction in cloudy air.

177 By separating active updrafts from the environment [e.g. *Siebesma and Cuijpers, 1995*],
 178 the turbulent flux can be written as

$$179 \quad F_\psi = \overline{\rho w' \psi'} = \rho a (1 - a) (w_u - w_e) (\psi_u - \psi_e) + \rho a \overline{w' \psi'^u} + \rho (1 - a) \overline{w' \psi'^e}, \quad (3)$$

180 where subscripts u and e indicate conditional averaging over active updrafts and the envi-
 181 ronment, respectively. w is vertical velocity and a is the area fraction of active updrafts.
 182 Since a is very small for the BOMEX case (Fig. 1a), we adopt the following highly ac-
 183 curate approximation in the rest of the paper: $(1 - a) \approx 1$ and $\psi_e \approx \bar{\psi}$. The first term
 184 on the RHS of Eq. 3 represents net transport by active updrafts and the compensating
 185 subsidence. Under the above approximation, it can be written as $M(\psi_u - \bar{\psi})$, where

186 $M = \rho a w_u$ is the convective mass flux. The second and third terms represent turbulent
 187 flux due to heterogeneities inside updrafts and the environment, respectively.

188 The EDMF model [e.g. *Siebesma et al.*, 2007; *Sušelj et al.*, 2012] parameterizes F_ψ as
 189 the sum of a mass flux component (MF) and an eddy-diffusivity component (ED),

$$190 \quad F_\psi \approx M(\psi_u - \bar{\psi}) - \rho K_\psi \frac{\partial \bar{\psi}}{\partial z}, \quad (4)$$

191 where K_ψ is the eddy diffusion coefficient. To describe the MF component in the EDMF
 192 approach, we use a bulk plume model, [e.g. *Siebesma et al.*, 2007]

$$193 \quad \frac{1}{M} \frac{\partial M}{\partial z} = \epsilon_\psi - d_\psi, \quad (5)$$

$$194 \quad \frac{\partial M \psi_u}{\partial z} = \epsilon_\psi M \bar{\psi} - d_\psi M \psi_u + \rho S_{\psi,u}, \quad (6)$$

196 where ϵ and d (m^{-1}) are the effective fractional entrainment and detrainment rates, re-
 197 spectively. In the cloud layer, the active updrafts are defined as cloudy grids with upward
 198 vertical velocity ($q_c > 0.01g \text{ kg}^{-1}$ and $w > 0 \text{ m s}^{-1}$). In the subcloud layer, they
 199 are defined as grids with w values in the top 1.3%-percentile, which is within the range
 200 (1% – 5%) suggested by *Siebesma et al.* [2003, 2007]. *Sušelj et al.* [2012] tested that the
 201 overall results of their EDMF model are fairly insensitive to the specified threshold of the
 202 percentile. The tracers in the updrafts have initial values at the lowest model level (z_1)
 203 as the horizontal mean added with an excess that scales with the surface flux ($F_{sfc,\psi}$),

$$204 \quad \psi_u(z_1) = \overline{\psi(z_1)} + \alpha \frac{F_{sfc,\psi}}{\sigma_w(z_1)}, \quad (7)$$

205 where σ_w is the standard deviation of w and $\alpha = 1.06$ is a scaling parameter from *Siebesma*
 206 *et al.* [2007]. Given the ψ values at the lowest level, we can integrate Eq. 5-6 upward to
 207 have the ψ_u values on all levels. Compared to many other parameterizations that treat
 208 the cloud layer and the subcloud layer separately, the EDMF model has the advantage

of providing a unified framework that connects the subcloud layer and the cloud layer smoothly. It has been operational in several GCMs and has shown significant improvements in the simulation of shallow clouds (e.g. marine stratocumulus and continental stratus [e.g. *Koehler, 2005*]).

The prognostic variables of the EDMF model (Eq. 4-7) are q_t and the liquid water static energy ($h_l = C_p T + gz - Lq_c$, where C_p is the specific heat at constant pressure and L is the latent heat of vaporization) for the thermodynamic aspect and ϕ_1 and ϕ_2 for the chemical aspect. The EDMF model requires specifying the parameters ϵ_ψ , d_ψ , and K_ψ for each tracer. One can diagnose these parameters by matching the LES and EDMF model results (i.e. collecting M , $\bar{\psi}$ and ψ_u from LES snapshots and solving Eq. 5-6 for ϵ_ψ and d_ψ ; collecting F_ψ from the LES and solving Eq. 4 for K_ψ with $-\rho K_\psi \frac{\partial \bar{\psi}}{\partial z}$ treated as the residual). *Siebesma et al.* [2003] showed that because of the strong correlation between q_t and h_l , their tracer parameters are very close to each other. Our analysis confirmed their conclusion: the normalized root-mean-square error between ϵ_{q_t} and ϵ_{h_l} is about 20%. As many parameterizations in CTMs do not have parameters for individual tracers, we evaluate the EDMF model with the same set of parameters diagnosed from q_t for both thermodynamic and chemical tracers. By doing so, we are considering the scenario that the EDMF model can “perfectly” represent the thermodynamic aspects of convection and clouds; thus, any errors in the chemical variables are due to the parameter dependence on tracers and deficiencies in the representation of aqueous reaction.

2.3. Treatments of the Aqueous Phase Reactions in the EDMF Model and Current CTMs

Effects of the aqueous reaction are considered here only within cloudy updrafts (R_u , equivalent to $-S_{\psi,u}$ in Eq. 6 for the reactive tracers), given the reaction rate in cloudy downdrafts being small. In the EDMF model, R_u is calculated using variables in cloudy updrafts,

$$R_{u,EDMF} = k\phi_{1u}\phi_{2u}q_{c,u}. \quad (8)$$

In other words, the effect of cloudy/clear-sky heterogeneity on the aqueous reaction is explicitly represented. Moreover, the transport and reactions of reactive tracers are calculated simultaneously as we integrate the bulk plume upward; therefore they are coupled. In addition, the mass exchange of reactive tracers between the environment and cloudy updrafts is through entraining/detraining mixing processes, which are deduced from and constrained by the thermodynamic tracer.

The above representation of aqueous reaction is more consistent with the real atmospheric processes. With the transport (Eq. 4-6) and the aqueous reaction (Eq. 8) parameterized, we can run the EDMF as a single-column model using Eq. 2. At each time step, Eq. 5-6 and Eq. 8 are first integrated upward to obtain ψ_u and $S_{\psi,u}$. Next, Eq. 4 gives the convective flux F_ψ . This information is then used in Eq. 2 to calculate the tracer mixing ratio profiles of the following time step. Since the parameters (ϵ , d , and K) are diagnosed from q_t using LES results, the EDMF model will reproduce the LES q_t perfectly and h_l near perfectly. Thus, we only simulate the chemical tracers with the single-column model and compare them against the LES results. The EDMF single-column model has

249 the same vertical grids as the LES and a time step of 4 seconds, due to the consideration
 250 of numerical stability and the representation of aqueous reaction.

251 Parameterizations in current CTMs usually treat the transport and reactions of chemical
 252 tracers in shallow cumuli as split processes. The tracer transport by sub-CTM-grid-scale
 253 convection and chemical reactions are calculated in separate modules. Moreover, it is
 254 common to use the CTM grid mean tracer concentrations to calculate the aqueous reaction
 255 in cloudy air,

$$256 \quad R_{u,CTM} = k\overline{\phi_1} \overline{\phi_2} q_{c,u}. \quad (9)$$

257 To estimate the potential errors due to process-splitting in many CTMs, we run the
 258 EDMF single column model as if the transport and reaction are separate as in the CTMs.
 259 Over a CTM time step (Δt_{CTM}), we first calculate the tracer transport tendencies using
 260 the EDMF model without aqueous reaction, then calculate the tracer tendencies due to
 261 aqueous reaction using Eq. 9. The profiles of ϕ_1 and ϕ_2 are updated using the total
 262 tendencies over Δt_{CTM} . Note that since we do not update tracer profiles during the split
 263 processes (as some CTMs do), the results do not depend on whether transport or aqueous
 264 reaction is calculated first. This is a more consistent comparison with the EDMF model.
 265 In Section 3.5, the results from this setting are compared with the EDMF model with
 266 transport and aqueous reaction coupled.

3. Results

267 We start with some basic characteristics of the BOMEX shallow cumuli in the LES
 268 (Fig. 1). The area fraction (a , Fig 1a) of the active updrafts is specified to be a constant
 269 (1.3%) in the subcloud layer, and decreases with height in the cloud layer. In the cloud

270 layer, the net mass flux M also decreases with height, but less than a because w_u increases
271 with height due to buoyancy acceleration. At the cloud base (around 550 m level), a and
272 M are discontinuous due to the different definitions of updrafts applied in the subcloud
273 layer and the cloud layer. Although not for the reactive tracers examined here, for other
274 tracers with strong vertical gradients near the cloud base, this discontinuity may induce
275 biases in the EDMF model. $q_{c,u}$ increases with height due to continuous condensation
276 as cloudy updrafts rise (Fig. 1b). The active updrafts are significantly moister than the
277 environmental mean, especially in the cloud layer (Fig. 1c). As cloudy updrafts rise,
278 turbulent mixing continuously entrains environmental air into cloudy updrafts, pushing
279 cloudy updrafts' properties toward the environmental air properties. Fig. 1d shows the
280 flux of total water, Fq_t , and its decomposition through Eq. 4. The convective flux of q_t
281 is mostly due to the ED component in the subcloud layer, while mostly due to the MF
282 component in the cloud layer. This supports the “mass flux approximation” used in many
283 convective parameterizations that approximates the total flux by the MF component in
284 the cloud layer. The EDMF model represents the residuals as an eddy diffusion process
285 naturally connected with the subcloud layer eddy diffusion, which dominates the flux
286 transport there.

287 Fig. 1e-f shows the parameters diagnosed from q_t and applied to the chemical tracers.
288 In the cloud layer, the diagnosed ϵ and d are consistent with results in previous studies
289 ([e.g. *Siebesma et al.*, 2003]). In the subcloud layer, ϵ and d are smaller, consistent with
290 the relatively constant M in the subcloud layer. K_{qt} , which is close to the results in
291 Fig. 11 of *Siebesma et al.* [2003], is very large in the subcloud layer, corresponding to the

292 strong turbulent mixing there that maintains nearly constant vertical profiles of q_t (and
 293 other tracers). K_{qt} is small in the cloud layer, corresponding to small ED flux there.

3.1. the Control Case

294 Now we examine the steady state chemical aspect in the control case of the LES sim-
 295 ulations (solid lines in Fig. 2). The ϕ_1 profiles (Fig. 2a) share similar features with the
 296 q_t profiles (Fig. 1c), because the source of ϕ_1 , like q_t , comes from the surface flux and
 297 thus ϕ_1 is well correlated with q_t . $\overline{\phi_1}$ and $\overline{\phi_2}$ are nearly constant with height in the sub-
 298 cloud layer due to the strong turbulent mixing there. ϕ_{1u} and ϕ_{2u} at the cloud base have
 299 similar values as $\overline{\phi_1}$ and $\overline{\phi_2}$ in the surface layer, because cloudy updrafts originate from
 300 the surface. Above the cloud base, ϕ_{1u} and ϕ_{2u} decrease with height due to the aqueous
 301 reaction and entrainment of environmental air having lower mixing ratios. Detrainment
 302 of ϕ_2 -depleted cloudy air leads to the decrease of $\overline{\phi_2}$ with height. This effect is balanced
 303 by the relaxation of ϕ_2 in the clear sky, leading to the intersection of $\overline{\phi_2}$ and ϕ_{2u} at around
 304 800 m height.

305 The convective fluxes of ϕ_1 and ϕ_2 and their decomposition are shown in Fig. 2c-d. F_{ϕ_2}
 306 is much smaller than F_{ϕ_1} in magnitude due to the small contrast of ϕ_2 in updrafts and
 307 environment (Fig. 2b). In the subcloud layer, the ED component dominates the total flux
 308 of both ϕ_1 and ϕ_2 . In the cloud layer, the MF component accounts for almost all of the
 309 total flux for ϕ_1 . For ϕ_2 , the MF and ED components are of comparable amplitudes but
 310 with opposite signs. As can be seen from Fig. 2c-d, the “mass flux approximation” is well
 311 satisfied for ϕ_1 , consistent with previous studies that examined the convective transport
 312 of surface-originated tracers [e.g. *Vilà-Guerau de Arellano et al., 2005*]. However, the

313 approximation is not well satisfied for ϕ_2 , suggesting that additional considerations are
 314 needed for non-surface-originated tracers.

315 The horizontally averaged reaction rate \bar{R} (Fig. 2e) peaks slightly above cloud base
 316 and then decreases with height, mainly due to the decrease of cloud fraction with height
 317 (Fig. 1a). R_u actually increases with height due to the increase of $q_{c,u}$ (figure not shown).
 318 Aqueous reaction in cloudy updrafts (aR_u) accounts for most of the total aqueous reac-
 319 tion. Thus, neglecting aqueous reaction in cloudy downdrafts in the EDMF model is an
 320 acceptable simplification for the shallow cumulus studied here. For other types of convec-
 321 tion with substantial area fraction of cloudy downdrafts, such as stratocumulus, aqueous
 322 reaction in cloudy downdrafts should also be considered.

323 The steady state results of the EDMF model (circles in Fig. 2) reproduce the LES
 324 results quite well. The matches of ϕ_1 and F_{ϕ_1} are particularly good (vertically averaged
 325 relative errors $< 5\%$). The EDMF model underestimates \bar{R} by about 11%, but this is
 326 mostly due to the neglect of the aqueous reaction in cloudy downdrafts. When compared
 327 to reactions only in cloudy updrafts (aR_u), the error in EDMF reduces to about 3%.
 328 The EDMF model also reproduces ϕ_2 and F_{ϕ_2} (vertically averaged relative errors $< 5\%$),
 329 although, with some biases in the shape of the profiles. It underestimates the ϕ_2 flux of
 330 the MF component in the upper levels and has almost zero ED ϕ_2 flux in the cloud layer.
 331 Due to the cancellation of biases, the discrepancies of F_{ϕ_2} between the EDMF and LES
 332 results are, fortunately, smaller than discrepancies in the individual components.

333 Although the EDMF model well reproduces the LES results of the control case, in
 334 Sections 3.2-3.4 we examine the underlying assumptions of the EDMF model that can

335 lead to errors in representing chemical transports and aqueous reactions, and understand
 336 the dependence of these errors under different chemical parameters or settings.

3.2. Errors in the Eddy Diffusivity Component

337 The EDMF model has non-negligible deficiencies in parameterizing non-surface-
 338 originated tracer ϕ_2 (Fig. 2b,d). Particularly, it has almost zero ED flux component
 339 in the cloud layer, due to the small K diagnosed from q_t . Fig. 1f also shows K diagnosed
 340 from ϕ_1 and ϕ_2 . The diffusivities (K) of the surface-originated tracer q_t and ϕ_1 are close
 341 to each other. However, K_{ϕ_2} shows quite different features from K_{q_t} .

342 In the subcloud layer, K_{ϕ_2} is about half of K_{q_t} , but the differences of K there do not
 343 affect the EDMF model too much. We have run the EDMF model with K_{q_t} doubled or
 344 halved in the subcloud layer. The resulting ϕ_1 and ϕ_2 are very close to the ones shown
 345 in Fig. 2. This is because in the subcloud layer, K is so large that its first effect is
 346 to maintain nearly constant tracer profiles with height. The vertical gradient of tracers
 347 is relatively small ($\frac{\partial \psi}{\partial z} \approx 0$). Sizable changes in K can easily be compensated by small
 348 adjustments of tracer vertical gradients in the model. The K parameter may be important
 349 for the thermodynamic variables (h_l and q_t), which in turn can affect the subcloud layer
 350 properties, such as the subcloud layer depth and the delicate convective inhibition near
 351 the cloud base. However, for passive chemical tracers that do not interact with convection,
 352 using K diagnosed from q_t is sufficient for parameterizing them in the subcloud layer.

353 In the cloud layer, K_{ϕ_2} has a singular point near the 1300 m level, corresponding to
 354 the local minimum of $\overline{\phi_2}$ there (Fig. 2b). Above that level, K_{ϕ_2} is negative, which is
 355 unphysical. Note that the “ED” flux in the LES (Fig. 2d) is actually calculated as the
 356 difference between the total flux and the flux due to the MF component. As seen from

Eq. 3-4, the EDMF model posits that $\rho a \overline{w' \psi'^u} + \rho(1-a) \overline{w' \psi'^e} \approx -\rho K_\psi \frac{\partial \overline{\psi}}{\partial z}$, under the assumptions that $\rho a \overline{w' \psi'^u}$ is small and the turbulence in the environment is random. Fig. 3 shows that $\rho a \overline{w' \phi_2'^u}$ is relatively small. The positive ϕ_2 flux of the “ED” component (, and thus the negative K_{ϕ_2}) is mostly due to transport in the subsiding shells (Fig. 3), which is defined here as grids within 200 m of the nearest cloudy updrafts edge, including both saturated and saturated air [Heus and Jonker, 2008]. The flux in the rest of the environment (quiescent environment) is very small. If we further increase the cloud shell size, for example to within 400 m of the updrafts edge, the ϕ_2 flux in the quiescent environment becomes slightly negative and follows the ϕ_2 gradient as eddy diffusion. The above analysis suggests that for non-surface-originated tracer ϕ_2 , the eddy diffusion cannot appropriately represent the non-MF component flux, and the subsiding shells of the shallow cumulus clouds should be included in the parameterization.

3.3. Errors Due to In-cloud Heterogeneities

Next, we move to the MF component (i.e. the bulk plume model) of the EDMF model, particularly the aqueous reaction rate in the cloud layer. The bulk plume model assumes that the environment and cloudy updrafts have uniform properties within each category (the top-hat approximation, [Siebesma and Cuijpers, 1995]). In other words, the bulk plume model explicitly distinguishes cloudy updrafts from the environment, but neglects the heterogeneities of air within cloudy updrafts and the environment, leading to errors in the calculation of the aqueous reaction. To estimate the relative importance of the heterogeneity within cloudy updrafts, we define a segregation error (γ_{seg} , with units of %) as the relative error due to the top-hat approximation when the cloudy updraft mean

378 properties are correctly predicted,

$$379 \quad \gamma_{seg} = \frac{\phi_{1u} \phi_{2u} q_{c,u} - \overline{\phi_{1,n} \phi_{2,n} q_{c,n}}}{\overline{\phi_{1,n} \phi_{2,n} q_{c,n}}}, \quad (10)$$

380 Neglecting second order terms, γ_{seg} can be written as

$$381 \quad \gamma_{seg} \approx -C_{\phi_1, q_c} \mu_{\phi_1} \mu_{q_c} - C_{\phi_2, q_c} \mu_{\phi_2} \mu_{q_c} - C_{\phi_1, \phi_2} \mu_{\phi_1} \mu_{\phi_2}, \quad (11)$$

382 where $C_{x,y}$ is the correlation coefficient between x and y , and μ_x is the coefficient of
 383 variation (the ratio of the standard deviation to the mean) of x . γ_{seg} with the opposite
 384 sign is very close to the intensity of segregation used in many previous studies [e.g. *Krol*
 385 *et al.*, 2000; *Vilà-Guerau de Arellano et al.*, 2005]. Here the segregation of tracers in clear
 386 sky and cloudy updrafts is already taken into account in the bulk plume model, so that
 387 γ_{seg} measures segregation of tracers inside cloudy updrafts.

388 The decomposition of γ_{seg} in the LES control case based on Eq. 11 is shown in the top
 389 row of Fig. 4. First, we examine the correlation coefficients in the upper-central panel.
 390 ϕ_1 is strongly positively correlated with q_c in cloudy updrafts (C_{ϕ_1, q_c} is close to 1), as
 391 expected. ϕ_2 and q_c are also positively correlated near the cloud base, implying that the
 392 most energetic subcloud-layer updrafts are enriched in the reactive tracers and moisture.
 393 As cloudy updrafts rise, the aqueous reaction of the reactive tracers with each other leads
 394 to the negative correlation between ϕ_1 and ϕ_2 . In addition, above the height where ϕ_{2u}
 395 and $\overline{\phi_2}$ intersect (around 800 m, Fig. 2b), entrainment has opposite effects on ϕ_2 and ϕ_1
 396 of cloud updrafts: it increases ϕ_2 but decreases ϕ_1 in cloud updrafts. As a result, C_{ϕ_1, ϕ_2}
 397 (and also C_{ϕ_2, q_c}) becomes more and more negative as the updrafts go up. μ_{q_c} is large
 398 near cloud base (the upper-right panel) is because $q_{c,u}$ is small. μ_{ϕ_1} and μ_{ϕ_2} are much
 399 smaller than μ_{q_c} , indicating that reaction in the control case is slow and leads to very weak

400 heterogeneities of ϕ_1 and ϕ_2 in cloudy updrafts. The upper-left panel plots the products
 401 of the correlation coefficients and coefficients of variation (i.e. the RHS terms of Eq. 11).
 402 In the control case, γ_{seg} is dominated by the RHS1 term (the covariance between ϕ_1 and
 403 q_c) because the in-cloud heterogeneity of ϕ_1 (μ_{ϕ_1}) is larger than that of ϕ_2 (μ_{ϕ_2}).

404 As the relative abundances of ϕ_1 and ϕ_2 change in experiments in group 1, the reaction
 405 timescale and strength of in-cloud heterogeneities of the reactive tracers also change. The
 406 decompositions of γ_{seg} for a ϕ_1 -dominant case (the case with $\phi_{2,ref}/\phi_{2,ref0} = 1/12$ and
 407 $\overline{\phi_1} \approx 400\overline{\phi_2}$) and a ϕ_2 -dominant case (the case with $\phi_{2,ref}/\phi_{2,ref0} = 12$ and $\overline{\phi_2} \approx 500\overline{\phi_1}$)
 408 are shown in row 2 and row 3 of Fig. 4, respectively. Compared to the control case, the
 409 correlation coefficients are qualitatively similar in all three cases, but μ_{ϕ_1} and μ_{ϕ_2} can
 410 vary significantly. When ϕ_1 is strongly dominant in cloudy updrafts, ϕ_2 reacts quickly
 411 and thus has a short lifetime. The fast reaction leads to low values and strong in-cloud
 412 heterogeneities of ϕ_2 , giving the large value of μ_{ϕ_2} (blue line in the right panel of row
 413 2), even though its updraft mean value is small. As a result, γ_{seg} is dominated by the
 414 covariance term between ϕ_2 and q_c (RHS2 term, blue line in the left panel of row 2).
 415 When ϕ_2 is strongly dominant in cloudy updrafts, based on the same argument, γ_{seg} is
 416 dominated by the covariance term between ϕ_1 and q_c (RHS1 term, red line in the left
 417 panel of row 3).

418 We can define a Damköhler number (D_a) [e.g. *Molemaker and Vilà-Guerau de Arellano,*
 419 *1998; Krol et al., 2000; Schumann, 1989*] as the ratio of the in-cloud residence time of air
 420 parcels in shallow convection (τ_{con}) to the reaction timescale (τ_{ϕ_1} and τ_{ϕ_2}) to characterize
 421 the influences of convection on the aqueous reaction,

$$422 \quad D_{a,\phi_{1,2}} = \frac{\tau_{con}}{\tau_{\phi_{1,2}}}. \quad (12)$$

423 D_a being far smaller than 1 indicates that the heterogeneity of reactive tracers in cloudy
 424 updrafts is small, and the updrafts mean is adequate for the calculation of reaction rate.
 425 D_a being close to or greater than 1 indicates that the segregation of reactive tracers in
 426 cloudy updrafts is significant and may need to be taken into account.

427 τ_{con} can be estimated by dividing the total cloudy air mass by total inflow,

$$428 \quad \tau_{con} = \frac{\int_{z_{cb}}^{z_{ct}} a\rho dz}{M(z_{cb}) + \int_{z_{cb}}^{z_{ct}} \epsilon M dz}. \quad (13)$$

429 Using ϵ_{qt} , this gives $\tau_{con} = 370$ s. Alternatively, *Neggers et al.* [2002] calculated the
 430 eddy turnover time of individual clouds as the cloud depth divided by the cloud-averaged
 431 maximum vertical velocity. They found that the BOMEX clouds with different cloud
 432 depth have a relatively constant eddy turnover time of about 400 s (see their Fig. 4),
 433 close to τ_{con} estimated here by Eq. 13. Note that τ_{con} can be much smaller than the
 434 life-time of a cumulus cloud ($\sim 10^3$ s), because a cumulus cloud is continuously fed with
 435 updrafts from subcloud layer. The reaction time scale of ϕ_1 in the cloud layer as a whole
 436 can be estimated as the total ϕ_1 divided by the total reaction rate in cloudy updrafts,

$$437 \quad \tau_{\phi_1} = \frac{\int_{z_{cb}}^{z_{ct}} a\rho\phi_{1u} dz}{\int_{z_{cb}}^{z_{ct}} a\rho R_u dz}. \quad (14)$$

438 τ_{ϕ_2} can be estimated in a similar way. The reaction timescale on a particular level may
 439 differ from the overall timescale estimated from Eq. 14. For the control case, this gives
 440 $\tau_{\phi_1} \approx 5 \times 10^3$ s and $\tau_{\phi_2} \approx 3 \times 10^3$ s.

441 To represent the overall segregation error in the cloud layer, we define Γ_{seg} as the ver-
 442 tically averaged γ_{seg} weighted by the product of the cloudy updraft fraction and density.
 443 Γ_{seg} and the D_a of reactive tracers for all cases in group 1 are summarized in Fig. 5. From
 444 left to right, the reaction regime changes from ϕ_1 -dominant to ϕ_2 -dominant. Correspond-

445 ingly, D_{a,ϕ_1} changes from $\sim 10^{-3}$ to ~ 1 , and D_{a,ϕ_2} changes from ~ 1 to $\sim 10^{-3}$ (Fig. 5b).
 446 Γ_{seg} is dominated by the covariances between q_c and the tracer with the smaller reaction
 447 timescale (larger D_a). Thus, Γ_{seg} is positive to the left end and negative to the right end.
 448 In either direction, the absolute value of Γ_{seg} increases as the larger D_a value between the
 449 two reactive tracers increases. As the larger D_a approaches and exceeds 1, which indicates
 450 the reaction time scale is close to or faster than the in-cloud residence timescale, in-cloud
 451 heterogeneities have greater impacts on the aqueous reaction, but errors are only about
 452 10% when $D_a \approx 1$. In the real atmosphere, in situations in which the SO_2 concentration
 453 dominates the H_2O_2 concentration, O_3 may take in charge and play a bigger role in the
 454 aqueous oxidation of SO_2 , resulting in reduced segregation between SO_2 and oxidants in
 455 cloudy updrafts.

3.4. Errors Due to Entrainment/Detrainment Rates

456 The dependence of entrainment/detrainment rates (ϵ/d) on tracers can lead to errors
 457 in the EDMF model. For q_t and h_l , because they are so well-correlated, their ϵ/d are
 458 almost identical [e.g. *Siebesma et al.*, 2003]. However, ϵ_{ϕ_1} and ϵ_{ϕ_2} diagnosed from the LES
 459 results show sizable differences from ϵ_{q_t} for the control case (Fig. 6a). Since ϵ and d are
 460 constrained by the mass-flux equation (Eq. 5, i.e. $\epsilon_{\phi_1} - d_{\phi_1} = \epsilon_{q_t} - d_{q_t}$), here we only focus
 461 on the discussion of ϵ . Because the reaction is slow in the control case ($D_{a,\phi_{1,2}} \approx 0.1$),
 462 the surface-originated tracer ϕ_1 has ϵ similar to but slightly smaller than ϵ of q_t . The
 463 intersection of ϕ_{2u} and $\overline{\phi_2}$ around 800 m (Fig. 2b) leads to the unrealistic oscillation and
 464 negative values of ϵ_{ϕ_2} around that height. The tracer dependence on ϵ is largely due to
 465 the aqueous reaction. The actual detrained (entrained) air seldom has the cloudy updraft
 466 mean (environmental mean) properties ([*Romps*, 2010; *Dawe and Austin*, 2011; *Nie and*

467 *Kuang, 2012b*]). Because of the aqueous reaction, the differences between $\phi_{1,2}$ in detrained
 468 cloudy updrafts and their mean values in the cloudy updrafts are different from those of
 469 q_t . Thus, detraining (entraining) the same amount of cloudy (environmental) air leads to
 470 different fractional changes of the environmental (bulk plume) $\phi_{1,2}$ and q_t .

471 We estimate the errors of R due to the tracer dependence of ϵ in the bulk plume model
 472 as follows. The bulk plume (Eq. 5-6) starts at cloud base with $\phi_{1,u}$ and $\phi_{2,u}$ diagnosed
 473 from LES. After integrating upward over each level, we calculate γ_{seg} on that level from
 474 the LES results with Eq. 11 and use it to correct R_u . With the errors due to in-cloud
 475 heterogeneities fixed, what is left of the errors of R_u is only due to the errors in the
 476 cloudy updrafts mean tracer values caused by the inaccurate ϵ/d . The bulk plume model
 477 is integrated to the cloud top. The relative differences between the resulting R_u and
 478 the LES R_u are vertically averaged with the weighting factor of a and density, giving an
 479 estimation of entrainment error (Γ_{ent} , with units of %). Because ϕ_{2u} and $\overline{\phi_2}$ are very
 480 close to each other (Fig. 2b), the differences between ϵ_{q_t} and ϵ_{ϕ_2} have little effect on the
 481 calculation of ϕ_{2u} . Analyses indicate that Γ_{ent} is dominated by the differences between
 482 ϵ_{ϕ_1} and ϵ_{q_t} ; therefore our discussions hereafter focus on ϕ_1 and ϵ_{ϕ_1} .

483 It is expected that Γ_{ent} is also related to D_a . As long as the reaction timescale is large
 484 compared to the in-cloud residence timescale ($D_a \ll 1$), reactive tracers behave similarly
 485 to conservative tracers and Γ_{ent} should be small. When the reaction timescale is close
 486 to or smaller than the in-cloud residence timescale, the aqueous reaction will have larger
 487 effects on ϵ , leading to larger Γ_{ent} . The cases in group 2, in which we vary k from 10^{-4} to
 488 10^{-1} , demonstrate the above argument. Fig. 6b shows the ϵ_{ϕ_1} for all cases in group 2. As
 489 k increases, ϵ_{ϕ_1} deviates further away from ϵ_{q_t} to more negative values. Fig. 7 shows Γ_{ent}

490 and D_a of the group 2 cases as a function of k . As k increases from 10^{-4} to 10^{-1} , D_{a,ϕ_1}
 491 increases from $\sim 10^{-2}$ to $\sim 10^{-1}$, and D_{a,ϕ_2} from $\sim 10^{-2}$ to ~ 1 . Consistently, as D_a
 492 increases and approaches 1, the absolute value of Γ_{ent} starts to increase sharply (Fig. 7a).
 493 Γ_{ent} is always negative because ϵ_{ϕ_1} is always smaller than ϵ_{q_t} due to the aqueous reaction.

494 The analyses in Section 3.3-3.4 show that for most of the cases examined, the aqueous
 495 reaction can be viewed as slow ($D_a \ll 1$) compared to convective timescale. Thus, errors in
 496 the aqueous reaction due to segregation and the dependence of entrainment/detrainment
 497 rates on tracers are small. The EDMF model with diagnosed parameters from q_t repro-
 498 duces the transport and reactions of ϕ_1 and ϕ_2 quite well.

3.5. Evaluating the operator-splitting error in CTMs

499 In this subsection, we evaluate the error due to operator-splitting that is used in many
 500 CTMs. This is done by running the EDMF model but with the transport and aqueous
 501 reaction calculated separately over a typical CTM time step, as introduced in Section 2.3.

502 Fig. 8 summarizes the mean tracer concentrations (vertically averaged from the surface
 503 to the cloud top level) and mean aqueous reaction rate (vertically averaged from the cloud
 504 base to the cloud top level) in all the cases in the two groups. We first examine the LES
 505 results in group 1 (Fig. 8a-c), in which the relative ratio between ϕ_1 and ϕ_2 decreases
 506 moving from left to right on the x axes. The dependence of $\overline{\phi_1}$ and $\overline{\phi_2}$ on the relative
 507 abundance of ϕ_1 and ϕ_2 (x axes) is consistent with the experiment designs (note that the
 508 y axes in Fig. 8a-b are logarithmic). Fig. 8c shows that the LES \overline{R} peaks when ϕ_1 and
 509 ϕ_2 are comparable in cloudy updrafts. The cases in group 2 (Fig. 8d-f) shows that as k
 510 increases, both $\overline{\phi_1}$ and $\overline{\phi_2}$ decrease while \overline{R} increases.

511 The EDMF model results (red markers in Fig. 8) match the LES results quite well for
 512 the three variables in all the cases. However, if the transport and aqueous reaction in the
 513 EDMF model are treated as separated operators as is done in many CTMs over ΔT_{CTM} (30
 514 minutes in the calculation shown in Fig. 8), the results (blue markers) show significant
 515 error. To provide a quantitative estimation of the errors, Fig. 9 shows the normalized
 516 root-mean-square errors (NRSME) of $\overline{\phi_1}$, $\overline{\phi_2}$, and \overline{R} for all cases in the two EDMF model
 517 settings. The open markers indicate the mean is underestimated by simple models, while
 518 the solid markers indicate the mean is overestimated. Consistent with previous analysis,
 519 when ϕ_2 becomes dominant (D_{a,ϕ_1} approaches 1), the NMSRE of $\overline{\phi_1}$ increases (Fig. 9a).
 520 The opposite holds when ϕ_1 becomes dominant (Fig. 9b). For the second group of
 521 experiments (Fig. 9 d-f), as k increases, D_{a,ϕ_1} and D_{a,ϕ_2} approach 1, consistent with the
 522 increases of the NMSREs. In all the cases, the error in the EDMF model is much greater
 523 if the transport and aqueous reaction are treated as separated operators than if they
 524 are calculated simultaneously. The errors due to operator splitting decrease as ΔT_{CTM}
 525 decreases (Fig. 10, taking the control case as an example). However, even if ΔT_{CTM}
 526 decreases to 4 seconds, the same of the sub-CTM time step, operator-splitting still leads
 527 to additional errors.

528 Although here we evaluate the errors due to the operator-splitting in CTMs using the
 529 EDMF model, this error is independent of the EDMF model and exists in other mass-
 530 flux-based convective parameterizations. On the other hand, a mass-flux-based convective
 531 parameterization can reduce this error by calculating tracer transport and aqueous reac-
 532 tions in updrafts simultaneously [e.g. Berg *et al.*, 2015].

3.6. Chemical Transient States

533 Although the above analyses are in chemical steady states, the EDMF model with
 534 diagnosed parameters also works well in transient states. In the following three transient
 535 cases ($k = 0, 10^{-3}, 10^{-1}$), the BOMEX case is initialized from hour 0 and runs for
 536 6 hours. The initial conditions of chemical tracers are ϕ_1 being zero and ϕ_2 being the
 537 reference value.

538 Fig. 11a-c shows the LES-simulated evolution of tracer profiles and reaction rate of the
 539 $k = 10^{-3}$ case. As time progresses, ϕ_1 builds up in the subcloud layer and is transported
 540 upward by convective updrafts. The aqueous reaction leads to the decrease of ϕ_2 in the
 541 cloudy layer; and the ϕ_2 -depleted air is entrained into the subcloud layer and decreases
 542 $\overline{\phi_2}$ there. \overline{R} becomes non-negligible at about hour 0.5 and continues to grow, due to the
 543 development of shallow cumuli and the building up of ϕ_1 . During the thermodynamical
 544 steady period (hour 3 to hour 6), there is considerable variability of cloud fraction, reflected
 545 as the variation of \overline{R} . This internal variability, however, can be reduced by increasing the
 546 LES domain size or averaging over an ensemble of simulations.

547 We run the EDMF model from hour 3 to hour 6, with the same entrainment/detrainment
 548 and the same eddy diffusivity parameters as the ones in previous subsections. The initial
 549 profiles of the reactive tracers are taken from the LES profiles at hour 3. The differences
 550 of $\overline{\phi_1}$ and $\overline{\phi_2}$ between the EDMF model and the LES results (Fig. 11d-e) are small. \overline{R}
 551 in the EDMF results shows smoother variation in time than it does in the LES results
 552 (color contour in Fig. 11f). The comparison of vertically averaged \overline{R} between the EDMF
 553 model and the LES (lower panel in Fig. 11f) shows that the EDMF model captures the
 554 LES results well. Fig. 12 shows the comparison of the hour 6 profiles from the LES and

555 the EDMF model (which also starts from hour 3) for the $k = 0$ and $k = 10^{-1}$ cases.
556 Without aqueous reaction ($k = 0$), more ϕ_1 is transported into cloudy layer (Fig. 12a).
557 With strong aqueous reaction ($k = 10^{-1}$), significant amounts of ϕ_1 are only found in the
558 subcloud layer (Fig. 12b), since ϕ_1 in cloudy updrafts quickly reacts near the cloud base
559 (Fig. 12d). In both cases, the EDMF model reasonably reproduces the LES results.

4. Conclusions and Discussions

560 The goal of this study is to improve the representation of aqueous phase reactions in
561 shallow cumuli in global models. An LES with an idealized chemical reaction mimicking
562 the aqueous oxidation of surface-originated SO_2 by H_2O_2 is used to guide simple models.
563 We show that the EDMF approach with a bulk plume model is a promising solution.
564 When entrainment/detrainment rates and eddy diffusivity are diagnosed using a conser-
565 vative thermodynamic tracer (e.g. q_t), the EDMF model represents the transport and
566 aqueous reactions of reactive tracers quite well over a wide range of parameters. The
567 eddy diffusion component of the EDMF model is sufficient for parameterizing surface-
568 originated chemical tracers, while it may neglect the tracer transport in the cloud shells
569 for non-surface-originated tracers. The bulk plume component of the EDMF approach
570 has two sources of errors: neglecting the heterogeneities within cloudy updrafts leads
571 to a segregation error between reactive tracers and cloud water, and the use of entrain-
572 ment/detrainment parameters derived from q_t on reactive tracers leads to an entrainment
573 error. Both of these errors are related to the reaction timescale. When the reaction is
574 slow compared to the in-cloud residence time of air parcels, the reactive tracers behave
575 like conservative tracers, so that the EDMF model that represents the conservative ther-
576 modynamic tracers well can also represent the reactive tracers well. When the reaction

577 timescale approaches the in-cloud residence time of air parcels, in-cloud heterogeneity
578 increases and the entrainment/detrainment rates of reactive tracers further deviate from
579 those derived using conserved variables, resulting in greater errors.

580 The errors due to operator-splitting are estimated by running the EDMF model in a
581 CTM-like configuration where the tracer transport and aqueous reactions are calculated
582 separately over a time step representative of CTMs, and the aqueous reaction calcula-
583 tions use horizontal mean (rather than updraft) tracer concentrations. The error due to
584 operator-splitting can be significant ($> 50\%$ for all cases examined here with a CTM time
585 step of 30 minutes), especially when the reaction is fast compared to the in-cloud residence
586 time. The error decreases as the CTM time step decreases, but remains larger than that
587 of the case with tracer transport and aqueous reactions calculated simultaneously in the
588 cloudy updrafts.

589 In this study, the parameters for the EDMF model are diagnosed from a conserved
590 thermodynamical tracer. In GCMs, the uncertainties in these parameters, and therefore
591 the parameterized convection, are still the leading source of errors for the representation
592 of atmospheric chemistry. However, these uncertainties may be reduced by diagnosing
593 convective parameters from the resolved convection of a cloud resolving model (CRM)
594 inside each GCM column, a method known as the super-parameterized GCMs [*Grabowski,*
595 *2001; Khairoutdinov and Randall, 2001*]. *Gustafson et al.* [2008] and *Wang et al.* [2011]
596 have already adopted this approach and applied it in aerosol-climate simulations. In this
597 study, we lend support to theirs, provide an evaluation of the approach in an idealized
598 setting, and analyze the sources of errors and their dependence on chemical reaction
599 regimes.

600 Although a bulk plume model is used in the EDMF model in this study, many con-
601 vection parameterizations use multiple plumes/parcels to represent cloudy updrafts [e.g.
602 *Berg and Stull, 2005; Nie and Kuang, 2012a; Sušelj et al., 2013*]. A multiple plume/parcel
603 representation allows heterogeneities within cloudy updrafts, which can improve the rep-
604 resentation of nonlinear microphysical processes [e.g. *Krueger et al., 1997; Nie and Kuang,*
605 *2012b; Tölle and Krueger, 2014*]. It can also potentially benefit the aqueous reactions by,
606 for example, accounting for the segregation between reactive tracers in cloudy updrafts
607 and having different entrainment/detrainment rates for each plume.

608 The current work focuses on the a non-precipitating shallow cumulus convection with
609 an idealized aqueous reaction. Future work is needed to include more realistic chemistry,
610 additional complexities in convection (e.g. precipitation, downdrafts, convective organiza-
611 tion and so forth), and their possible interactions (e.g. aerosol-cloud interaction, [*Berner*
612 *et al., 2013; Wyant et al., 2015; Berg et al., 2015*]).

613 **Acknowledgments.** The authors thank Jessica Kunke for improving writing of the
614 manuscript. Comments from Mary Barth and two anonymous reviewers substantially
615 improved the paper. The numerical simulations presented were obtained and stored on
616 the Harvard Odyssey cluster. The data can be accessed upon contacting the authors
617 (jn2460@columbia.edu). JN acknowledges support from the Lamont Postdoctoral Fellow-
618 ship. ZK acknowledges support from NSF grants AGS-1062016, AGS-1260380, and the
619 Office of Biological and Environmental Research of the U.S. Department of Energy under
620 grant DE-SC0008679 as part of the ASR program.

References

- 621 Alexander, B., R. J. Park, D. J. Jacob, Q. B. Li, R. M. Yantosca, J. Savarino, C. C. W.
622 Lee, and M. H. Thiemens (2005), Sulfate formation in sea-salt aerosols: Constraints
623 from oxygen isotopes, *J. Geophys. Res.*, *110*, doi:10.1029/2004JD005659.
- 624 Barth, M. C., P. J. Rasch, J. T. Kiehl, C. M. Benkovitz, and S. E. Schwartz (2000), Sulfur
625 chemistry in the National Center for Atmospheric Research Community Climate Model:
626 Description, evaluation, features, and sensitivity to aqueous chemistry, *J. Geophys. Res.*,
627 *105*, 1387–1415.
- 628 Benkovitz, C. M., S. E. Schwartz, M. P. Jensen, and M. A. Miller (2006), Attribution of
629 modeled atmospheric sulfate and SO₂ in the Northern Hemisphere for June/July 1997,
630 *Atmos. Chem. Phys.*, *6*, 4723–4738.
- 631 Berg, L. K., and R. B. Stull (2005), A Simple Parameterization Coupling the Convective
632 Daytime Boundary Layer and Fair-Weather Cumuli, *J. Atmos. Sci.*, *62*, 1976–1988.
- 633 Berg, L. K., C. M. Berkowitz, J. C. Barnard, G. Senum, and S. R. Springston (2011),
634 Observations of the first aerosol indirect effect in shallow cumuli, *Geophys. Res. Lett.*,
635 *38*, L03809.
- 636 Berg, L. K., M. Shrivastava, R. C. Easter, J. D. Fast, E. G. Chapman, Y. Liu, and R.
637 A. Ferrare (2015), A new WRF-Chem treatment for studying regional-scale impacts of
638 cloud processes on aerosol and trace gases in parameterized cumuli, *Geosci. Model Dev.*,
639 *8*, 409–429.
- 640 Berner, A. H., C. S. Bretherton, R. Wood, and A. Muhlbauer (2013), Marine boundary
641 layer cloud regimes and POC formation in an LES coupled to a bulk aerosol scheme,
642 *Atmos. Chem. Phys.*, *13*, 12549–12572.

- 643 Daum, P. H., T. J. Kelly, S. E. Schwartz, and L. Newman (1984), Measurements of the
644 chemical composition of stratiform clouds, *Atmos. Environ.*, *18*, 2671–2684.
- 645 Dawe, J. T. and P. H. Austin (2011), The Influence of the Cloud Shell on Tracer Budget
646 Measurements of LES Cloud Entrainment, *J. Atmos. Sci.*, *68*, 2909–2920.
- 647 Easter, R. C., S. J. Ghan, Y. Zhang, R. D. Saylor, E. G. Chapman, N. S. Laulainen,
648 H. Abdul-Razzak, L. R. Leung, X. Bian, and R. A. Zaveri (2004), MIRAGE:
649 Model description and evaluation of aerosols and trace gases, *J. Geophys. Res.*, *109*,
650 doi:10.1029/2004JD004571.
- 651 Ghan, S. J., X. Liu, R. C. Easter, R. Zaveri, P. J. Rasch, J.-H. Yoon, and B. Eaton (2012),
652 Toward a Minimal Representation of Aerosols in Climate Models: Comparative Decom-
653 position of Aerosol Direct, Semidirect, and Indirect Radiative Forcing, *J. Climate*, *25*,
654 6461–6476.
- 655 Grabowski, W. W. (2001), Coupling Cloud Processes with the Large-Scale Dynamics
656 Using the Cloud-Resolving Convection Parameterization (CRCP), *J. Atmos. Sci.*, *58*,
657 978–997.
- 658 Gustafson, W. I., L. K. Berg, R. C. Easter, and S. J. Ghan (2008), The Explicit-Cloud
659 Parameterized-Pollutant hybrid approach for aerosolcloud interactions in multiscale
660 modeling framework models: tracer transport results *Environ. Res. Lett.*, *3*(2), 025005.
- 661 Heus, T. and H. J. J. Jonker (2008), Subsiding Shells around Shallow Cumulus Clouds,
662 *J. Atmos. Sci.*, *65*, 1003–1018.
- 663 Holland, J. Z., and E. M. Rasmusson (1973), Measurement of atmospheric mass, energy,
664 and momentum budgets over a 500-kilometer square of tropical ocean, *Mon. Weather*
665 *Rev.*, *101*, 44–55.

- 666 Jacob, D. J., et al. (1997), Evaluation and intercomparison of global atmospheric transport
667 models using Rn-222 and other short-lived tracers, *J. Geophys. Res.*, *102*, 5953–5970.
- 668 Jacob, P., T.M. Tavares, V.C. Rocha, and D. Klockow (1990), Atmospheric H₂O₂ field
669 measurements in a tropical environment: Bahia, Brazil, *Atmos. Environ.*, *124A*, 377–
670 382.
- 671 Jöckel, P., H. Tost, A. Pozzer, C. Brhl, J. Buchholz, L. Ganzeveld, P. Hoor, A. Kerkweg,
672 M.G. Lawrence, R. Sander, B. Steil, G. Stiller, M. Tanarhte, D. Taraborrelli, J. van
673 Aardenne, and J. Lelieveld (2006), The atmospheric chemistry general circulation model
674 ECHAM5/MESSy1: consistent simulation of ozone from the surface to the mesosphere,
675 *Atmos. Chem. Phys.*, *6*, 5067–5104.
- 676 Kazil, J., H. Wang, G. Feingold, A. D. Clarke, J. R. Snider, and A. R. Bandy (2011),
677 Modeling chemical and aerosol processes in the transition from closed to open cells
678 during VOCALS-REx, *Atmos. Chem. Phys. Discuss.*, *11*, 7491–7514.
- 679 Khairoutdinov, M. F., and D. A. Randall (2001), A cloud-resolving model as a cloud
680 parameterization in the NCAR Community Climate System Model: Preliminary results,
681 *Geophys. Res. Lett.*, *28*, 3617–3620.
- 682 Khairoutdinov, M. F., and D. A. Randall (2003), Cloud-resolving modeling of the ARM
683 summer 1997 IOP: Model formulation, results, uncertainties and sensitivities, *J. Atmos.*
684 *Sci.*, *60*, 607–625.
- 685 Kim, S. W., M. C. Barth, and M. Trainer (2012), Influence of fair-weather cumulus clouds
686 on isoprene chemistry, *J. Geophys. Res.*, *117*, doi:10.1029/2011JD017099.
- 687 Koehler, M. (2005), Improved prediction of boundary layer clouds, *ECMWF Newsletter*,
688 *104*, ECMWF, Reading, United Kingdom, 18–22.

- 689 Krol, M. C., M. J. Molemaker, and J. Vila-Guerau de Arellano (2000), Effects of turbu-
690 lence and heterogeneous emissions in photochemically active species in the convective
691 boundary layer, *J. Geophys. Res.*, *105*, 6871–6884.
- 692 Krueger, S. K., C. Su, and P. A. McMurtry (1997), Modeling Entrainment and Finescale
693 Mixing in Cumulus Clouds, *J. Atmos. Sci.*, *54*, 2697–2712.
- 694 Lawrence, M. G., and J. R. Philip (2005), Tracer Transport in Deep Convective Updrafts:
695 Plume Ensemble versus Bulk Formulations, *J. Atmos. Sci.*, *62*, 2880–2894.
- 696 Liu, X., J. E. Penner, and M. Herzog (2005), Global modeling of aerosol dynamics: Model
697 description, evaluation, and interactions between sulfate and nonsulfate aerosols, *J.*
698 *Geophys. Res.*, *110*, D18206, doi:10.1029/2004JD005674.
- 699 Molemaker, M. J. and J. Vilà-Guerau de Arellano (1998), Control of Chemical Reactions
700 by Convective Turbulence in the Boundary Layer, *J. Atmos. Sci.*, *55*, 568–579.
- 701 Neggers, R. A. J., A. P. Siebesma, and H. J. J. Jonker (2002), A multiparcel model for
702 shallow cumulus convection, *J. Atmos. Sci.*, *69*, 1655–1668.
- 703 Nie, J., and Z. Kuang (2012a), Responses of shallow cumulus convection to large-scale
704 temperature and moisture perturbations: a comparison of large-eddy simulations and a
705 convective parameterization based on stochastically entraining parcels, *J. Atmos. Sci.*,
706 *69*, 1936–1956.
- 707 Nie, J., and Z. Kuang (2012b), Beyond bulk entrainment and detrainment rates: a
708 new framework for diagnosing mixing in cumulus convection, *Geophys. Res. Lett.*, *39*,
709 L21803.
- 710 Rasch, P. J., M. C. Barth, J. T. Kiehl, S. E. Schwartz, and C. M. Benkovitz (2000), A
711 description of the global sulfur cycle and its controlling processes in the National Center

- 712 for Atmospheric Research Community Climate Model, Version 3, *J. Geophys. Res.*, *105*,
713 1367–1385.
- 714 Romps, D. M. (2010), A Direct Measure of Entrainment, *J. Atmos. Sci.*, *67*, 1908–1927.
- 715 Sakugawa, H., I.R. Kaplan, W. Tsai, and Y. Cohen (1990), Atmospheric hydrogen per-
716 oxide, *Environ. Sci. Technol.*, *24*, 1452–1462.
- 717 Schumann, U. (1989), Large-eddy simulation of turbulent diffusion with chemical reactions
718 in the convective boundary layer, *Atmos. Environ.*, *23*, 1713–1727.
- 719 Seinfeld, J. H. and S. N. Pandis (1998), *Atmospheric chemistry and physics: from air*
720 *pollution to climate change*, J. Wiley, New Jersey. Page 366.
- 721 Siebesma, A. P., and J. W. M. Cuijpers (1995), Evaluation of parametric assumptions for
722 shallow cumulus convection, *J. Atmos. Sci.*, *52*, 650–666.
- 723 Siebesma, A. P., et al. (2003), A large eddy simulation intercomparison study of shallow
724 cumulus convection, *J. Atmos. Sci.*, *60*, 1201–1219.
- 725 Siebesma, A.P., P.M.M. Soares and J. Teixeira (2007), A combined Eddy Diffusivity Mass
726 Flux approach for the convective boundary layer, *J. Atmos. Sci.*, *64*, 1230–1248.
- 727 Sušelj, K., J. Teixeira, and G. Matheou (2012), Eddy Diffusivity/Mass Flux and Shallow
728 Cumulus Boundary Layer: An Updraft PDF Multiple Mass Flux Scheme, *J. Atmos.*
729 *Sci.*, *69*, 1513–1533.
- 730 Sušelj, K., J. Teixeira, D. Chung (2013), A Unified Model for Moist Convective Boundary
731 Layers Based on a Stochastic Eddy-Diffusivity/Mass-Flux Parameterization, *J. Atmos.*
732 *Sci.*, *70*, 1929–1953.
- 733 Tölle, M. H., and S. K. Krueger (2014), Effects of entrainment and mixing on droplet size
734 distributions in warm cumulus clouds, *J. Adv. Model. Earth Syst.*, *6*, 281–299.

- 735 Verma, S., O. Boucher, M. S. Reddy, H. C. Upadhyaya, P. Le Van, F. S. Binkowski, and O.
736 P. Sharma (2007), Modeling and analysis of aerosol processes in an interactive chemistry
737 general circulation model, *J. Geophys. Res.*, *112*, D03207, doi:10.1029/2005JD006077.
- 738 Vilà-Guerau de Arellano, J., S.-W. Kim, M. C. Barth, and E. G. Patton (2005), Transport
739 and chemical transformations influenced by shallow cumulus over land, *Atmos. Chem.*
740 *Phys.*, *5*, 3219–3231.
- 741 Wang, M., et al. (2011), The multi-scale aerosol-climate model PNNL-MMF: model de-
742 scription and evaluation, *Geosci. Model Dev.*, *4*, 137–168.
- 743 Wu, S., L. J. Mickley, D. J. Jacob, J. A. Logan, R. M. Yantosca, and D. Rind (2007), Why
744 are there large differences between models in global budgets of tropospheric ozone? *J.*
745 *Geophys. Res.*, *112*, D05302, doi:10.1029/2006JD007801.
- 746 Wyant, M. C., and coauthors (2015), Global and regional modeling of marine boundary
747 layer clouds and aerosols in the marine boundary layer during VOCALS: The VOCA
748 Intercomparison, *Atmos. Chem. Phys.*, *15*, 153–172.

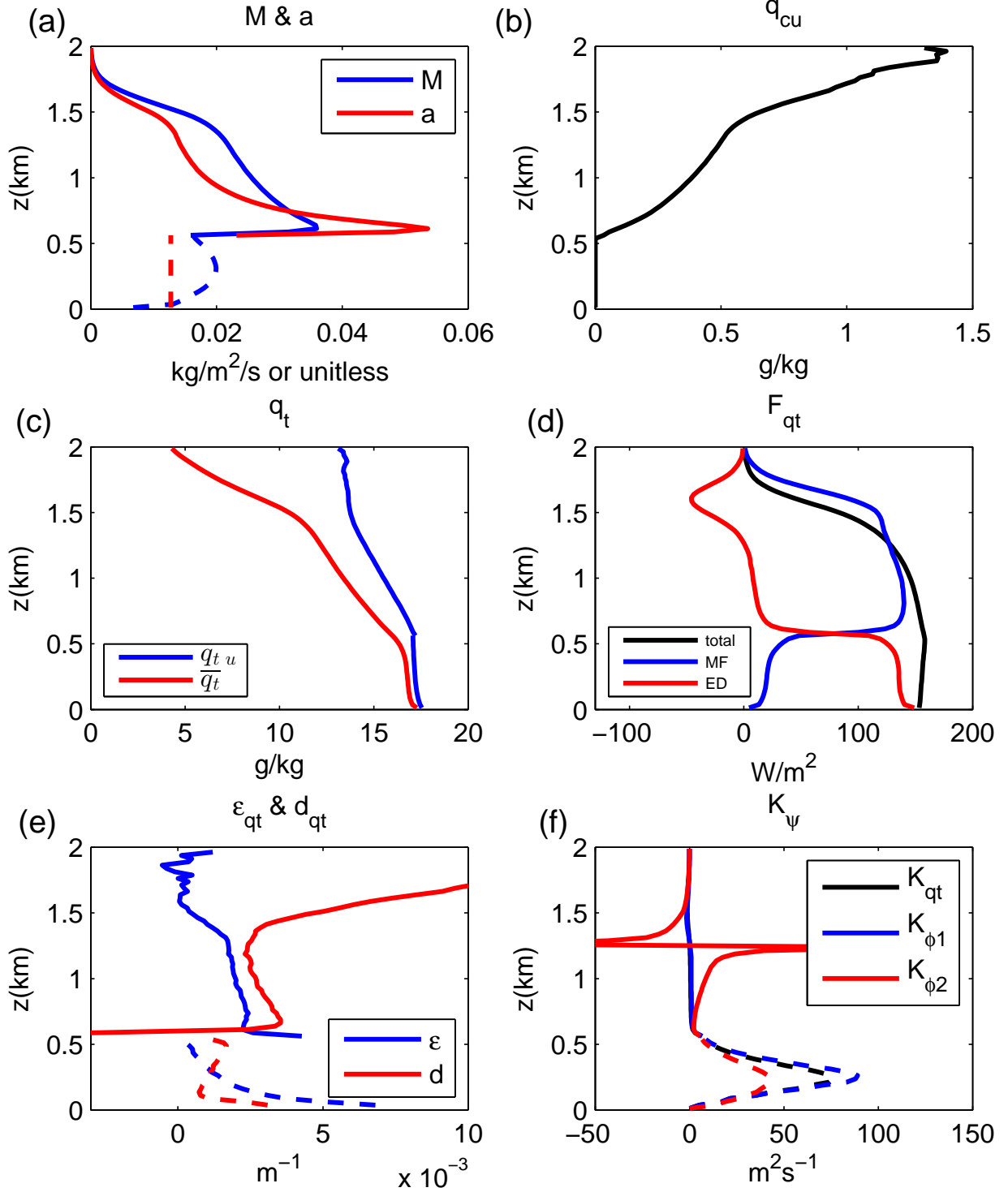


Figure 1. The LES simulated (a) active updrafts area fraction a and mass flux M , (b) $q_{c,u}$, (c) total water content q_t in updrafts and environment, (d) F_{q_t} and its decomposition, (e) ϵ and d diagnosed from q_t , and (f) K diagnosed from q_t , ϕ_1 , and ϕ_2 . The dashed line indicates values in the subcloud layer.

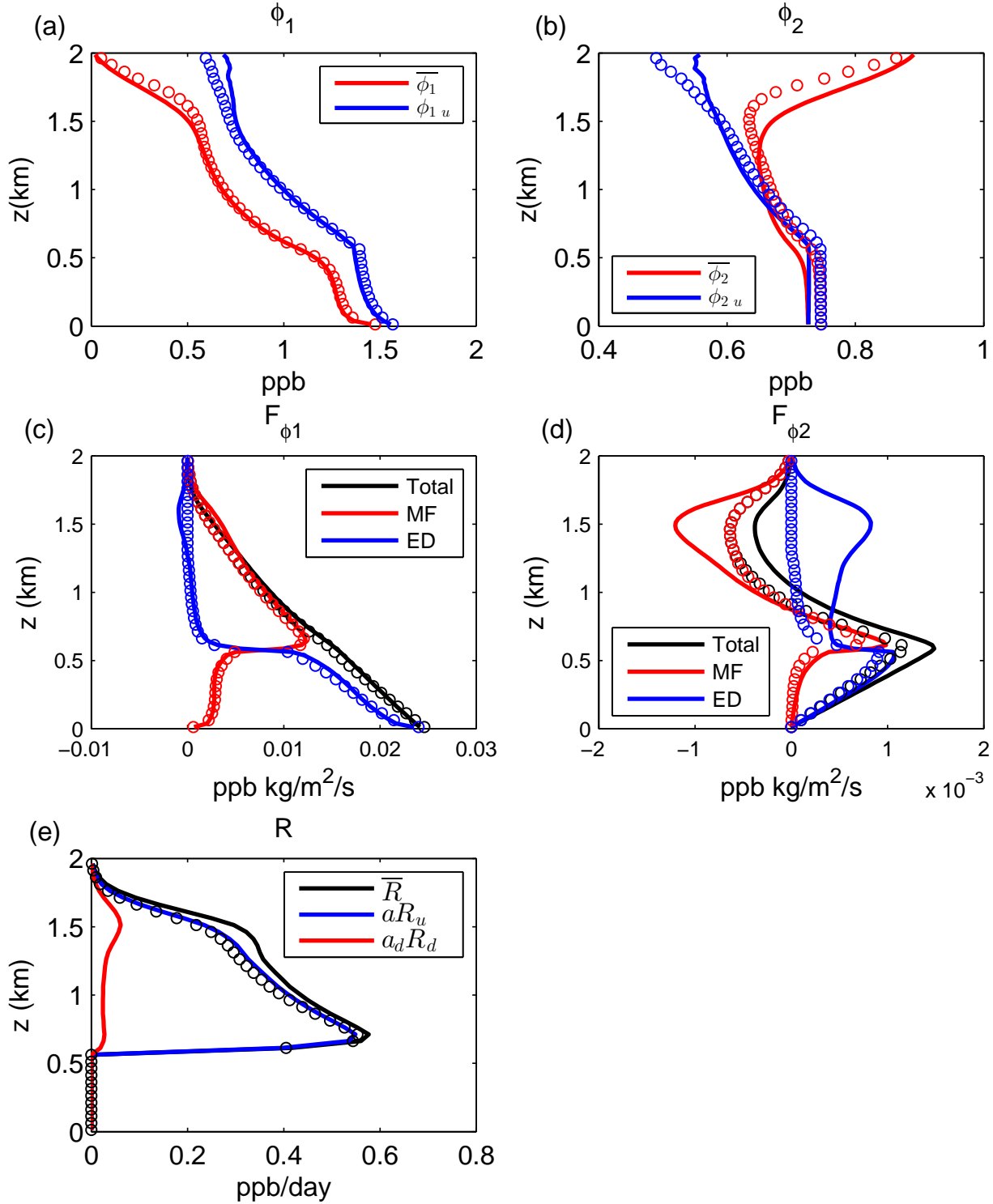


Figure 2. The control case steady state (a) $\overline{\phi_1}$ and ϕ_{1u} , (b) $\overline{\phi_2}$ and ϕ_{2u} , (3) F_{ϕ_1} and its decomposition, (4) F_{ϕ_2} and its decomposition, (5) aqueous reaction rate and its portion in cloudy updrafts and downdrafts. The color lines are the LES results, and the color circles are the EDMF model results.

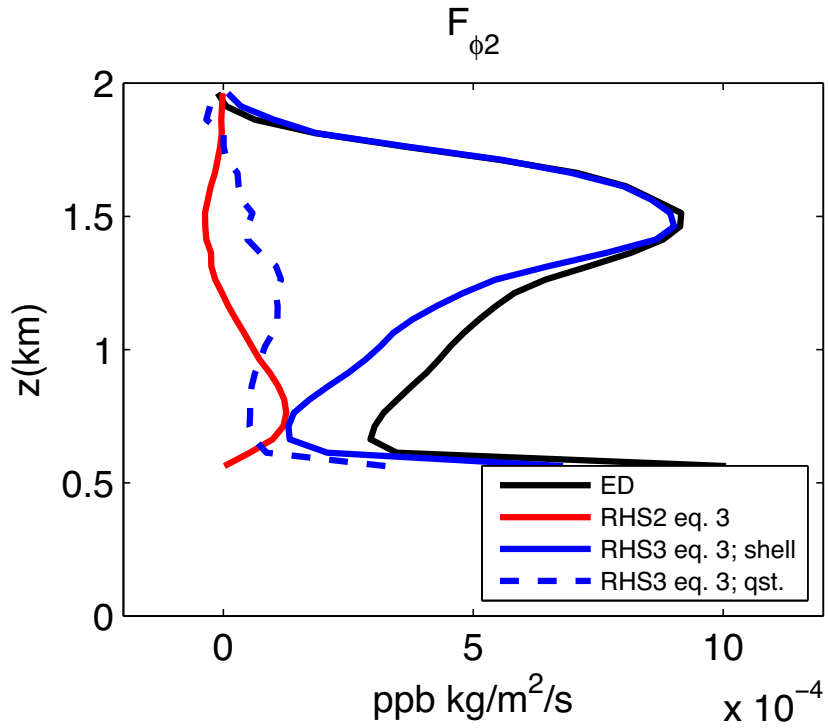


Figure 3. The decomposition of the LES ϕ_2 flux of the “ED” component (black line) into contributions from the cloudy updrafts (red line), the subsiding shells (blue solid line), and the quiescent environment (blue dashed line).

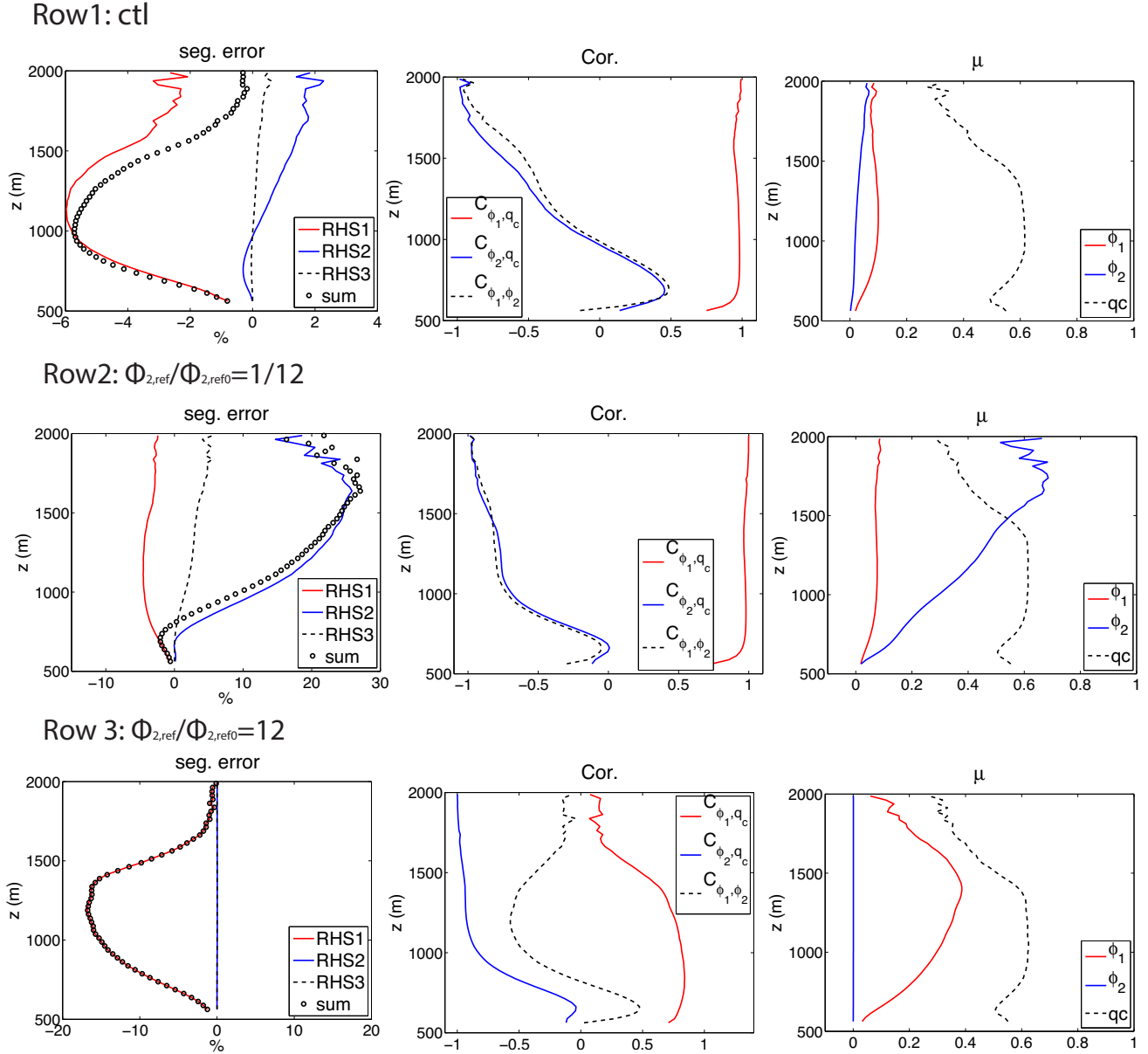


Figure 4. Left column: the segregation error and its decomposition based on Eq. 11. Central column: the correlation coefficients between ϕ_1 , ϕ_2 , and q_c in cloudy updrafts. Right column: the coefficients of variation of ϕ_1 , ϕ_2 , and q_c . From the top row to the bottom row, they are for the control case, $\phi_{2,ref}/\phi_{2,ref0} = 1/12$ case, and $\phi_{2,ref}/\phi_{2,ref0} = 12$ case, respectively.

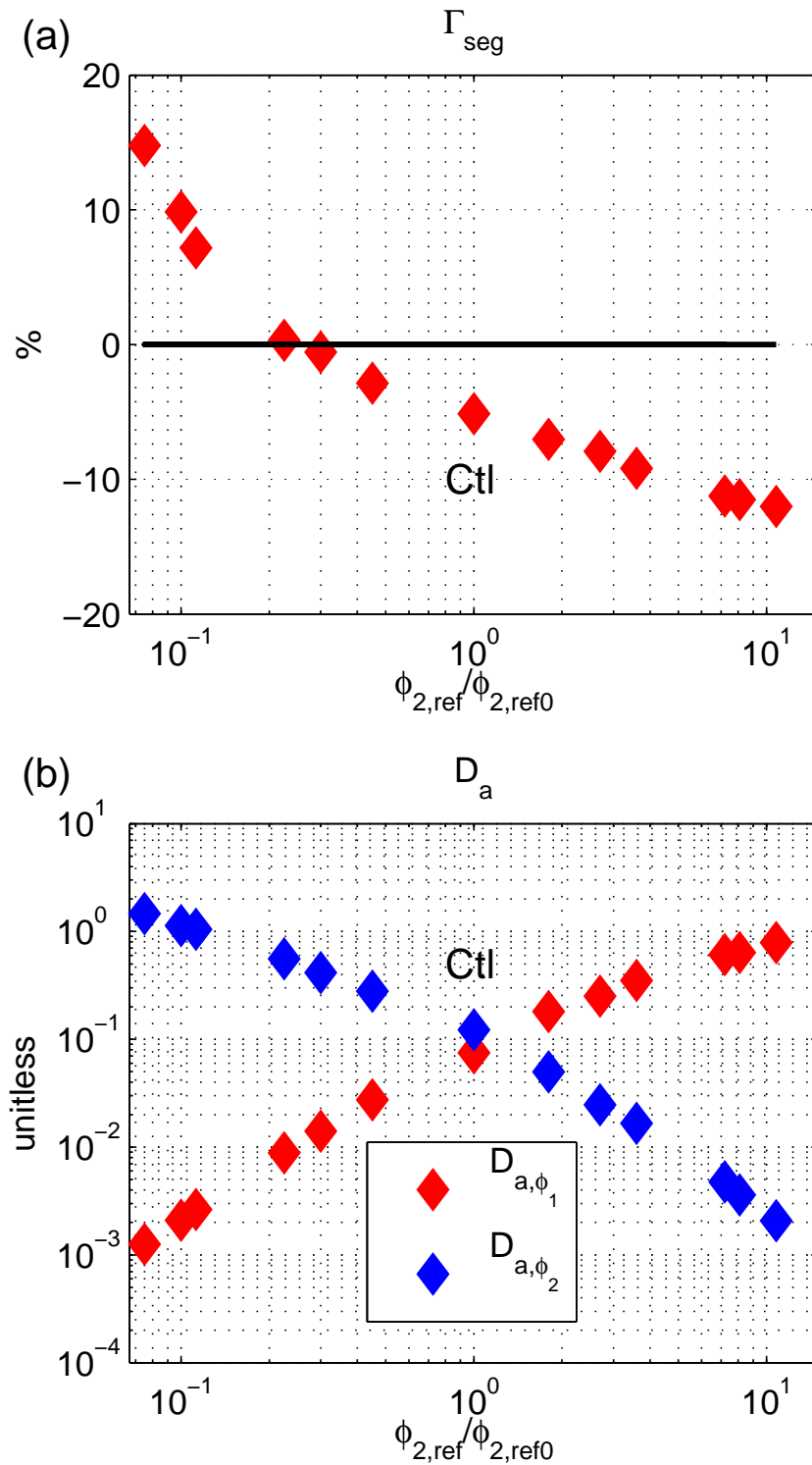


Figure 5. (a) Γ_{seg} , and (b) D_{a,ϕ_1} and D_{a,ϕ_2} of the cases in group 1.

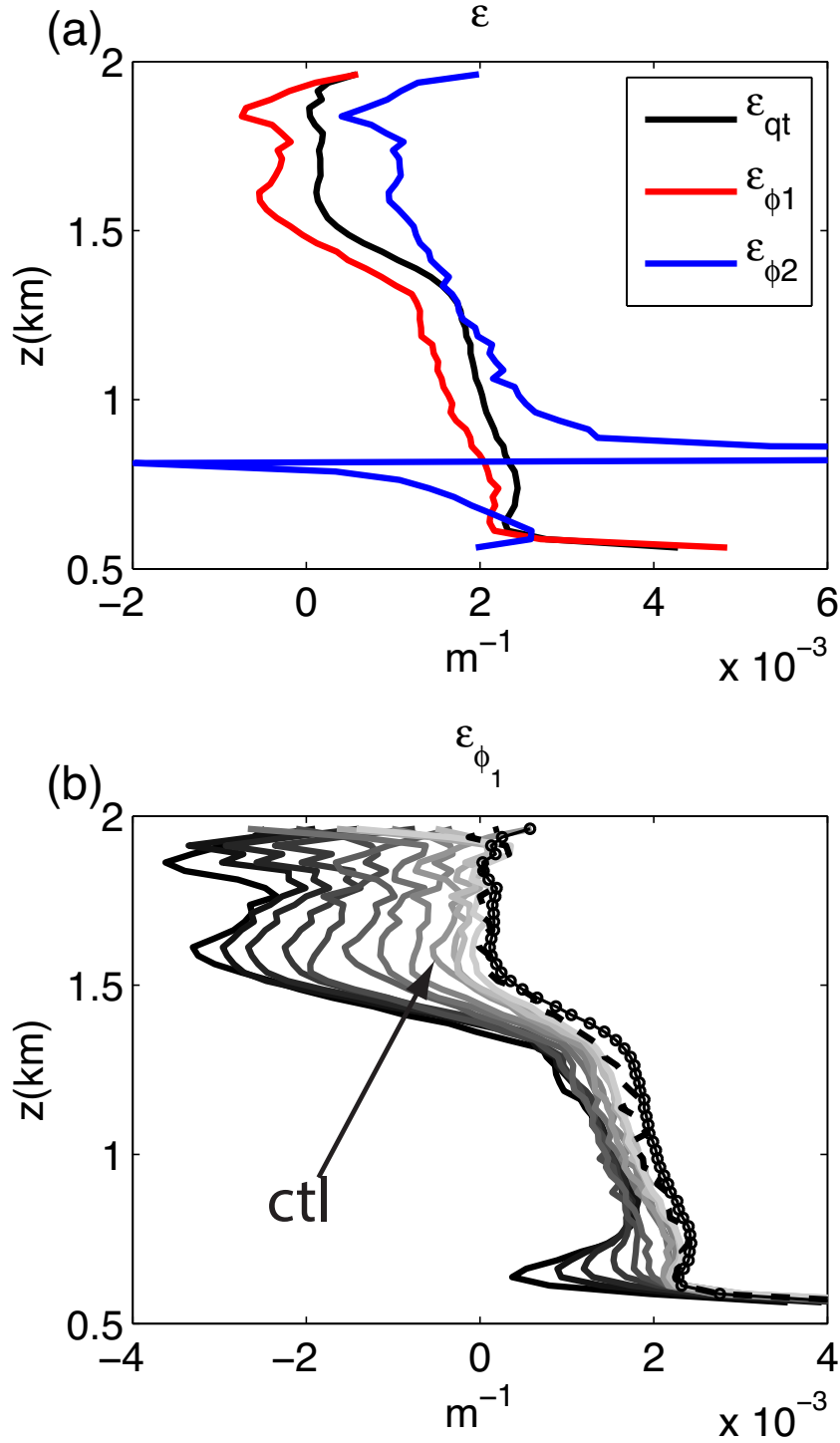


Figure 6. (a): the control case ϵ_{qt} , $\epsilon_{\phi 1}$ and $\epsilon_{\phi 2}$ that are diagnosed from their conservation equations. (b): each line indicates $\epsilon_{\phi 1}$ of one case in the group 2. Lines from lighter to darker are cases from small k (10^{-4}) to large k (10^{-1}). The dashed line corresponds $k = 0$ case. ϵ_{qt} is also plotted as circle for reference.

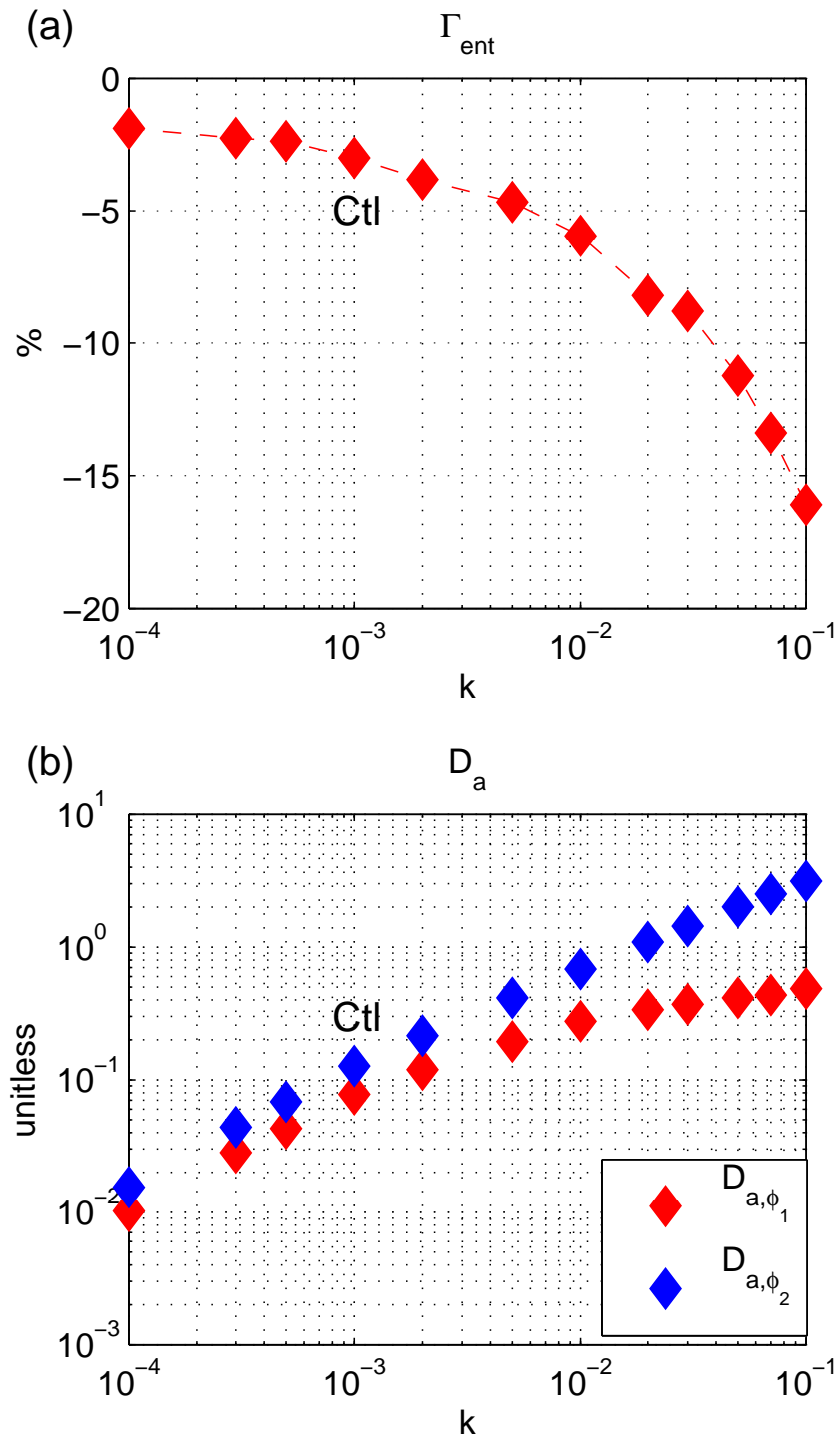


Figure 7. (a) Γ_{ent} , and (b) D_{a,ϕ_1} and D_{a,ϕ_2} of the cases in group 2.

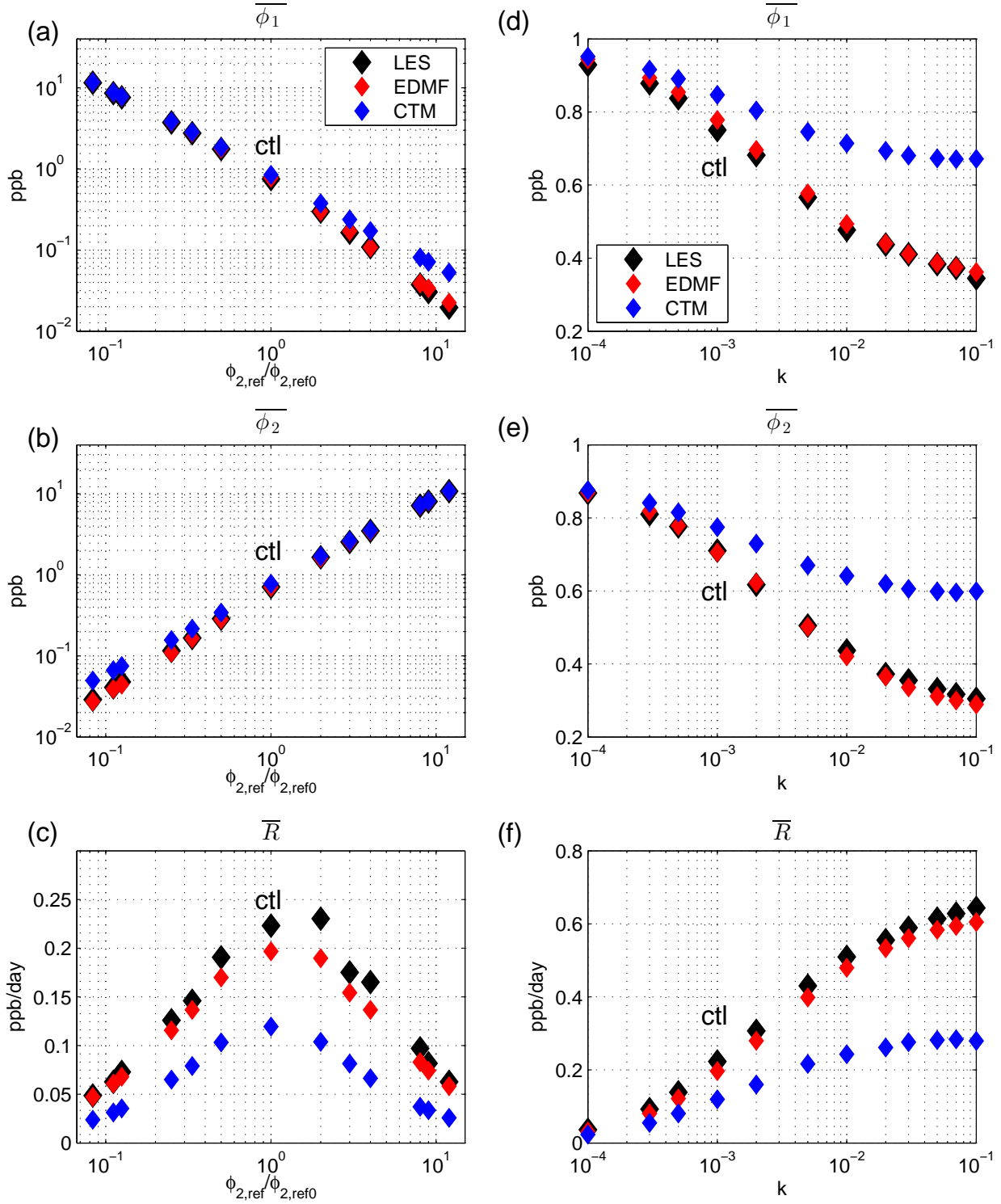


Figure 8. From top to bottom, each panel shows the LES (black), the EDMF model (red), and the EDMF model with operators-splitting (blue) results of the vertical averaged $\overline{\phi_1}$ (top), $\overline{\phi_2}$ (middle), and \overline{R} (bottom) respectively. The left column is for the cases in group 1, and the right column is for the cases in group 2.

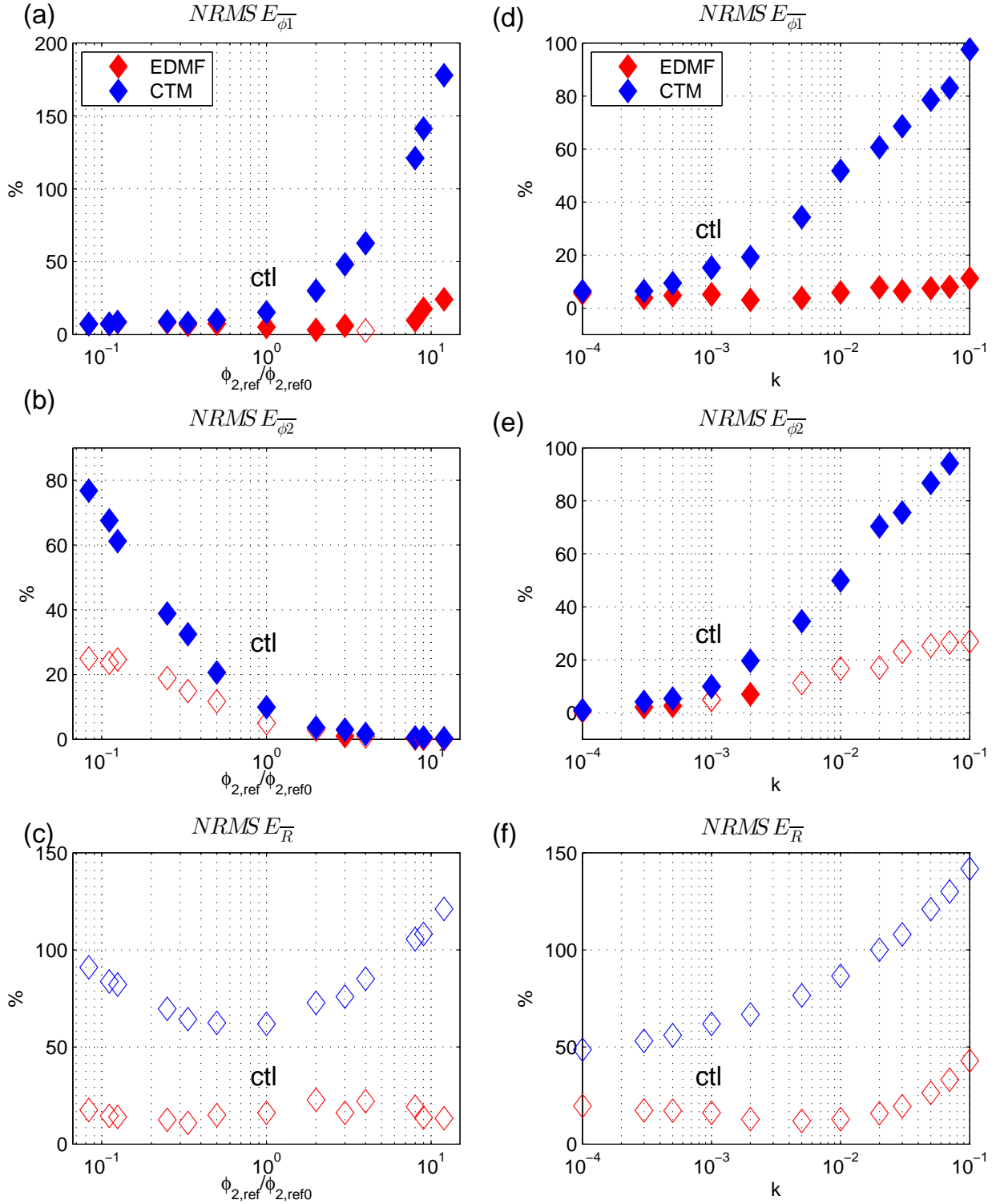


Figure 9. The NRMSE of $\overline{\phi_1}$ (top), $\overline{\phi_2}$ (middle), and \overline{R} (bottom) of the results of the EDMF model (red) and the EDMF model with operators-splitting (blue). Solid (open) marker indicates the vertical averaged variables is overestimated (underestimated) by the simple model comparing to the LES results. The left column is for the cases in group 1, and the right column is for the

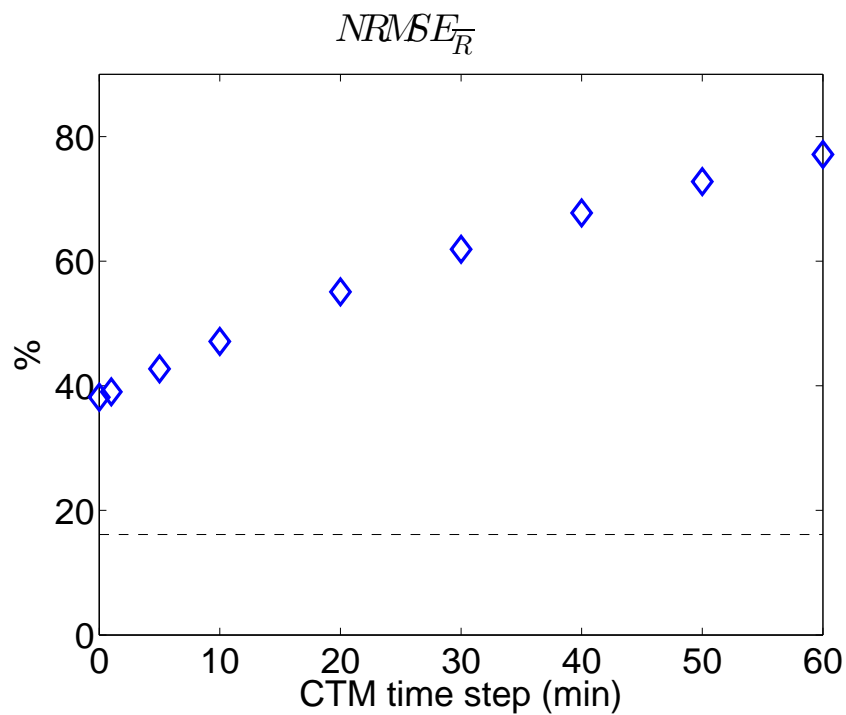


Figure 10. The control case NRMSE of \bar{R} in the EDMF model with operators-splitting as functions of ΔT_{CTM} . The dashed line indicates NRMSE of \bar{R} in the EDMF model with tracer transport and aqueous reactions calculated simultaneously.

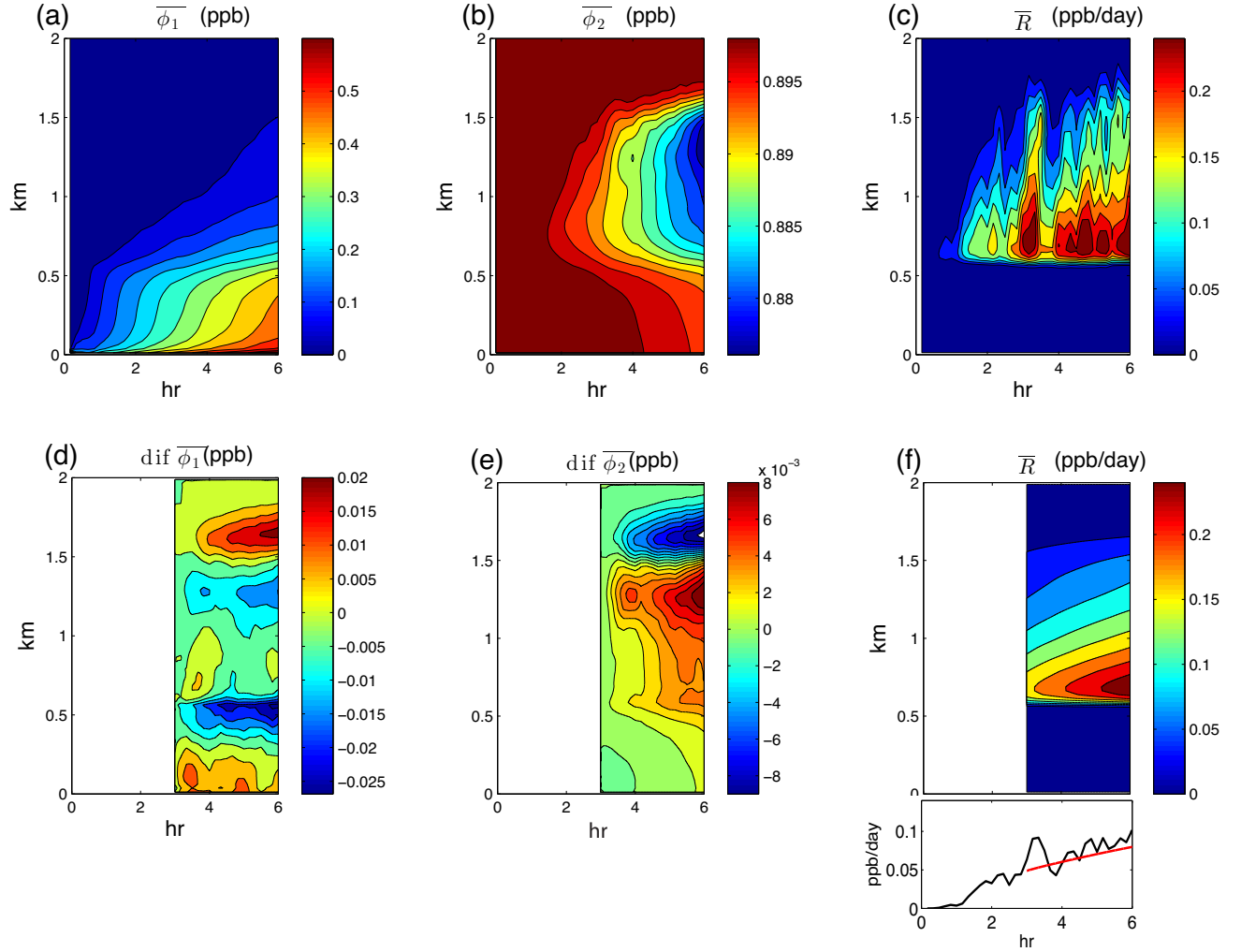


Figure 11. The comparison between the LES and EDMF model in the transient case with $k = 10^{-3}$. Upper lines: time evolution of (a) $\overline{\phi_1}$, (b) $\overline{\phi_2}$, and (c) \overline{R} of the LES results. Lower lines: differences of (d) $\overline{\phi_1}$ and (e) $\overline{\phi_2}$ between the EDMF model and the LES results. (f) shows \overline{R} in the EDMF model results, with the upper panels being the time evolution and the lower panel being vertically averaged time series (red line). In the lower panel of (f), the LES time series is also shown as the black line.

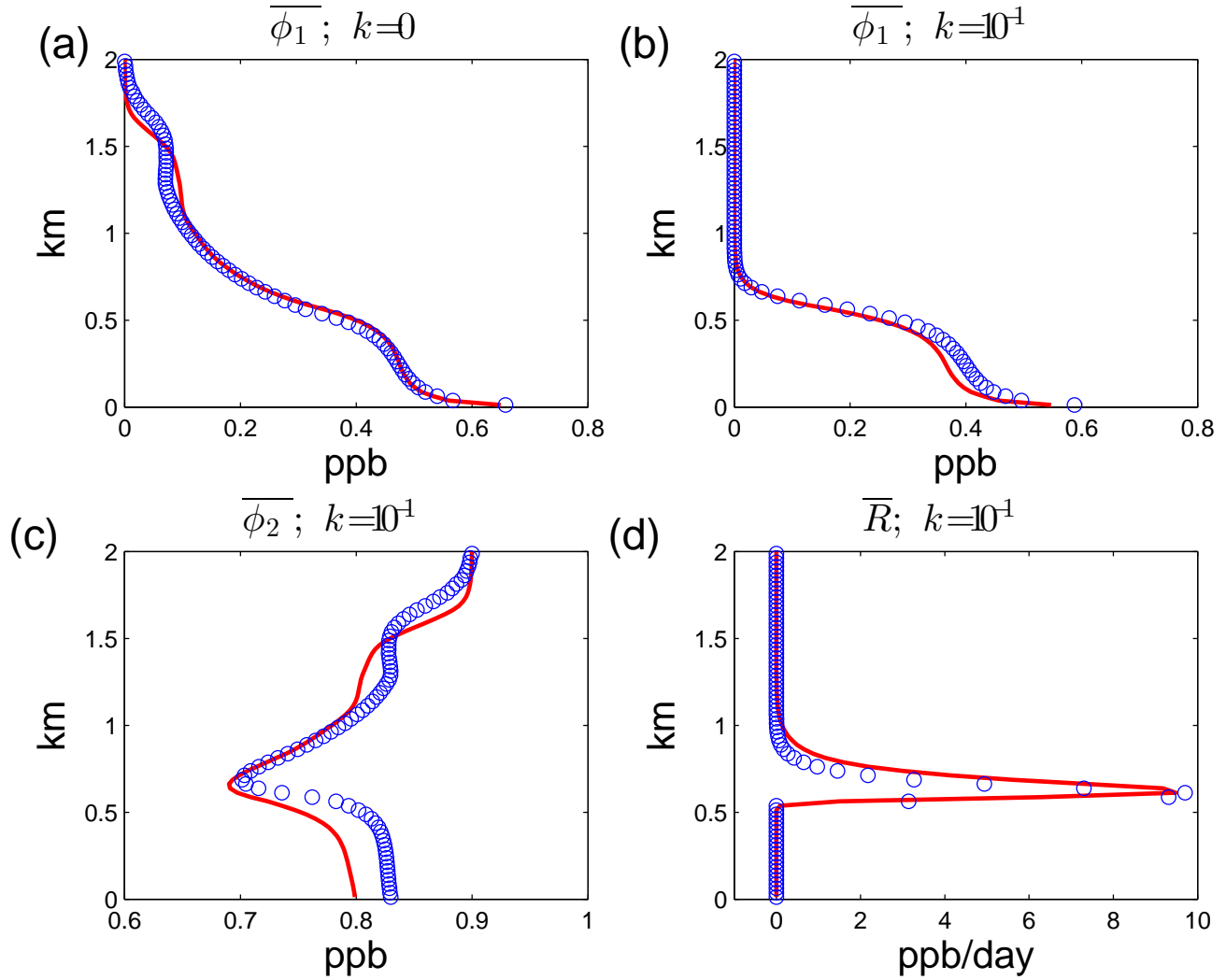


Figure 12. The hour 6 profiles of (a) $\overline{\phi_1}$ of the $k = 0$ case; (b) $\overline{\phi_1}$, (c) $\overline{\phi_2}$, and (d) \overline{R} of the $k = 10^{-1}$ case. The red solid lines are the LES results, and the blue circles are the EDMF model results.